Thesis for the degree of Licentiate of Engineering

Quasi-Single Mode VCSELs for Longer-Reach Optical Interconnects

Erik Haglund

Photonics Laboratory
Department of Microtechnology and Nanoscience (MC2)
Chalmers University of Technology
Göteborg, Sweden, 2013

Quasi-Single Mode VCSELs for Longer-Reach Optical Interconnects

Erik Haglund

Göteborg, August 2013

© Erik Haglund, 2013

Technical Report MC2-258
ISSN 1652-0769

Chalmers University of Technology
Department of Microtechnology and Nanoscience (MC2)
Photonics Laboratory, SE-412 96 Göteborg, Sweden
Phone: +46 (0) 31 772 1000

Printed by Chalmers reproservice, Chalmers University of Technology
Göteborg, Sweden, August, 2013

Quasi-Single Mode VCSELs for Longer-Reach Optical Interconnects

Erik Haglund
Photonics Laboratory
Department of Microtechnology and Nanoscience (MC2)
Chalmers University of Technology
SE-412 96 Göteborg, Sweden

Abstract

The vertical-cavity surface-emitting laser (VCSEL) is the standard light source in optical interconnects connecting racks in supercomputers and datacenters hosting services such as online data sharing, storage and processing. VCSELs have numerous advantages such as low power consumption, fast direct modulation at low currents, circular output beam for efficient fiber coupling and low-cost fabrication. However, today's commercial optical interconnects, operating at around 10 Gbit/s over up to 300 m of multimode fiber, have insufficient speed and reach for future datacenters.

The goal of this work has been to extend the maximum reach of GaAs-based 850 nm VCSEL-based optical interconnects. Recently developed high-speed VCSELs featuring strained InGaAs quantum wells and multiple oxide layers are highly transverse multimode with large root-mean-square (RMS) spectral widths around 1 nm. This leads to problems with chromatic and modal fiber dispersion, limiting the maximum reach to around 100 m at 25 Gbit/s. By using quasi-single mode VCSELs with a side-mode suppression ratio of ~15-20 dB and RMS spectral widths around 0.3 nm, the reduced dispersive effects enable extended reach at high data rates. Two different techniques to reduce the spectral width are investigated. By using a small oxide aperture, the number of modes guided by the VCSEL waveguide is significantly reduced. A 3 µm oxide aperture VCSEL was used to transmit 22 Gbit/s over 1100 m of OM4 fiber. However, small aperture devices have high resistance and relatively low output power. The spectral width of larger aperture VCSELs can be reduced by etching a shallow surface relief that induces a mode selective loss to suppress higher order modes. In effect, the etched feature acts as an integrated mode filter. A 6 µm oxide aperture surface relief VCSEL enabled transmission at 20 Gbit/s over 2000 m of fiber, setting a new bit-rate-distance product record for directly modulated 850 nm VCSEL links. Benefits and drawbacks of both methods are discussed and compared.

Keywords: vertical-cavity surface-emitting laser, spectral width, high-speed modulation, quasi-single mode, mode control, oxide aperture, mode filter

List of Papers

This thesis is based on the following appended papers:

[A] R. Safaisini, K. Szczerba, **E. Haglund**, P. Westbergh, J. S. Gustavsson, A. Larsson, and P. Andrekson, "20 Gbit/s error-free operation of 850 nm oxide-confined VCSELs beyond 1 km of multimode fibre," *Electron. Lett.*, vol. 48, no. 19, pp. 1225-1227, Sept. 2012.

[B] R. Safaisini, K. Szczerba, P. Westbergh, **E. Haglund**, B. Kögel, J. S. Gustavsson, A. Larsson, and P. Andrekson, "High-Speed 850 nm Quasi-Single-Mode VCSELs for Extended-Reach Optical Interconnects," *J. Opt. Commun. Netw.*, vol. 5, no. 7, pp. 686-695, July 2013.

[C] **E. Haglund**, Å. Haglund, P. Westbergh, J. S. Gustavsson, B. Kögel, and A. Larsson, "25 Gbit/s transmission over 500 m multimode fibre using 850 nm VCSEL with integrated mode filter," *Electron. Lett.*, vol. 48, no. 9, pp. 517-518, April 2012.

[D] **E. Haglund**, Å. Haglund, J. S. Gustavsson, B. Kögel, P. Westbergh, and A. Larsson, "Reducing the spectral width of high speed oxide confined VCSELs using an integrated mode filter," *Proceedings of SPIE Vertical-Cavity Surface-Emitting Lasers XVI*, vol. 8276, Feb. 2012.

[E] R. Safaisini, **E. Haglund**, P. Westbergh, J. S. Gustavsson, and A. Larsson, "20 Gb/s data transmission over 2 km multimode fibre using 850 nm mode filter VCSELs," *Manuscript*, Aug. 2013.

Related publications and conference contributions by the author:

[F] **E. Haglund**, Å. Haglund, P. Westbergh, R. Safaisini, J. S. Gustavsson, B. Kögel, and A. Larsson, "Low Spectral Width High-Speed VCSELs," Poster presented at the *International Nano-Optoelectronic Workshop (iNOW)*, Aug. 2011.

[G] P. Westbergh, **E. Haglund**, J. S. Gustavsson, Å. Haglund, B. Kögel, and A. Larsson, "High speed VCSELs for short reach communication," *European Semiconductor Laser Workshop*, Sept. 2011.

[H] P. Westbergh, R. Safaisini, **E. Haglund**, B. Kögel, J. S. Gustavsson, A. Larsson, M. Geen, R. Lawrence, and A. Joel, "High-speed 850 nm VCSELs with 28 GHz modulation bandwidth operating error-free up to 44 Gbit/s," *Electron. Lett.*, vol. 48, no. 18, Aug. 2012.

[I] P. Westbergh, R. Safaisini, **E. Haglund**, B. Kögel, J. S. Gustavsson, A. Larsson, and A. Joel, "High-speed 850 nm VCSELs with 28 GHz modulation bandwidth," *European Semiconductor Laser Workshop*, Sept. 2012.

[J] **E. Haglund**, Å. Haglund, P. Westbergh, J. S. Gustavsson, B. Kögel, and A. Larsson, "Mode-filtered semiconductor lasers enable longer-reach optical interconnects," *SPIE Newsroom*, Oct. 2012.

[K] **E. Haglund**, P. Westbergh, R. Safaisini, B. Kögel, Å. Haglund, J. S. Gustavsson, K. Szczerba, and A. Larsson, "High-speed lasers for optical interconnects," Poster presented at the *Swedish Optics and Photonics Days*, Stockholm, Sweden, Oct. 2012.

[L] P. Westbergh, R. Safaisini, **E. Haglund**, J. S. Gustavsson, A. Larsson, M. Geen, R. Lawrence, and A. Joel, "High-Speed Oxide Confined 850-nm VCSELs Operating Error-Free at 40 Gb/s up to 85°C," *IEEE Photon. Techn. Lett.*, vol. 25, no. 8, pp. 768-771, April 2013.

[M] **E. Haglund**, P. Westbergh, E. P. Haglund, R. Safaisini, J. S. Gustavsson, K. Szczerba, Å. Haglund, and A. Larsson, "850 nm datacom VCSELs for higher-speed and longer-reach transmission," Presented at the *European VCSEL Day*, Lausanne, Switzerland, June 2013.

[N] P. Westbergh, E. P. Haglund, **E. Haglund**, R. Safaisini, J. S. Gustavsson, and A. Larsson, "High-speed 850 nm VCSELs operating error free up to 57 Gbit/s," *Electron. Lett.*, vol. 49, no. 16, pp. 1021-1023, Aug. 2013.

Acknowledgement

There are many who have supported me during the last three years, making this work possible. I would first like to thank my supervisor and examiner Prof. Anders Larsson for letting me work in this exciting field and for his support, always ready for discussions with an open door. I would like to thank Åsa Haglund for cheerfully sharing her vast experience in VCSELs, listening to crazy ideas and also for, together with Petter Westbergh, giving me an excellent introduction to the fine art of VCSEL processing. I am also grateful to Johan S. Gustavsson for simulations, Rashid Safaisini for rewarding collaboration on difficult projects, Benjamin Kögel for teaching me about courage, Krzysztof Szczerba for helping me narrow my knowledge gap on fibers and Jörgen Bengtsson for reminding me that lunch breaks are breaks.

My office mate Martin Stattin deserves many thanks for his support in dealing with problems both small and large. I am very lucky to work at the Photonics Laboratory with so many great past and present Fiber Guys, Opto Dudes and Sheila Galt. Finally, I want to thank my family and friends for always being there for me.

This research was financially supported by the European FP7 project VISIT (224211) and the Swedish Foundation for Strategic Research (SSF) project LASTECH. IQE Europe is gratefully acknowledged for supplying the epitaxial material.

Erik Haglund

Göteborg
August 2013

Table of Contents

Abstract **i**

List of Papers **iii**

Acknowledgement **v**

1 Introduction **1**
1.1 History of VCSELs 2
1.2 Organization of Thesis 2

2 VCSELs in Optical Interconnects **3**
2.1 Transmission Standards 4
2.2 Data Transmission in Multimode Fiber 5
2.3 State-of-the-Art 6

3 VCSEL Design and Characteristics **9**
3.1 VCSEL Cavity 9
3.2 Active Region 12
3.3 Optical and Electrical Confinement 12
3.4 Spectral Characteristics 15
3.5 Dynamic Properties 17

4 Quasi-Single Mode VCSELs **19**
4.1 Small Oxide Aperture 20
4.2 Surface Relief Mode Filter 21
4.2.1 Effects on Static Characteristics 23

5 High-Speed Characterization **25**
5.1 Small-Signal Modulation Response 25
5.2 Large-Signal Modulation and Data Transmission 25

6 VCSEL Fabrication **27**
6.1 Lithography 27
6.2 Thin Film Deposition 28
6.3 Etching 29
6.4 Wet Oxidation 30
6.5 High-Speed VCSEL Process 30
6.5.1 Surface Relief Processing 32

7 Outlook and Future Directions **33**

8 Summary of Papers **35**

References **39**

A Process Plan **49**

Papers A–E **59**

Chapter 1

Introduction

The concept of *cloud computing* is today already changing the way we use the Internet. One of the most important effects of this development is that the user's computer, tablet and smartphone are mainly used as terminals where the user can access information and input commands, while the data storage and processing is located on servers in massive datacenters distributed around the world. Cloud computing services include search engines, social networking, online data storage, processing and sharing, backup and gaming. These services require a high degree of interaction between the servers, thereby demanding a reliable, high-bandwidth, short latency and low-cost web of interconnects linking the servers together [1]. Electrical interconnects with copper cables have high attenuation at high frequencies, limiting their performance to 10 Gbit/s over just a few meters [2]. The most promising solution is to use fiber-optical links (called optical interconnects) instead. A single datacenter or supercomputer may today use 100 000's of optical interconnects making this a very cost-sensitive application [3]. Because of this, low-cost vertical-cavity surface-emitting lasers (VCSELs) are used in the transmitters with multimode fiber (MMF) as the transmission medium. VCSEL-based optical interconnects have additional advantages over copper cables such as being insensitive to electromagnetic interference, taking up less space, thus allowing efficient flow of cooling air, as well as a lower energy consumption [2]. The majority of these links are shorter than 100 m in length, but as datacenters are growing larger, often into multi-building complexes, longer links up to 2 km will be required [4]. Long-reach optical interconnects for ∼500-2000 m currently employ InP-based 1310 nm DFB (distributed feedback) lasers and single mode fiber (SMF). Using 850 nm VCSELs instead could potentially

lower cost and energy consumption. The main challenge in designing longer links with 850 nm VCSELs is the relatively wide optical spectrum of a standard high-speed VCSEL, leading to severe signal distortion due to dispersion in the MMF. This is prevented by using low spectral width single mode or quasi-single mode VCSELs.

1.1 History of VCSELs

The concept of a vertical-cavity semiconductor laser was first proposed in 1977 by Professor K. Iga from Tokyo Institute of Technology, who two years later also demonstrated the first VCSEL lasing under pulsed operation at 77 K [5, 6]. This first VCSEL more resembled a "vertical edge emitter" with a relatively long cavity and metal coated mirrors. The first reports of room temperature operation of VCSELs were published in 1989 [7, 8]. During the 1990's VCSEL research really took off and the first commercial VCSELs came on the market in the middle of the decade. VCSEL-based short-reach fiber-optic links for data communication were introduced in 1996 [9]. Today 850 nm GaAs-based VCSEL technology is extensively utilized in short-reach optical communication links, with 95% of all optical networking applications $<$1000 m using multimode fiber and 850 nm VCSELs [10]. The largest volume market for VCSELs is, however, in optical computer mice where 850 nm VCSELs can be used to track movement on uniform surfaces with higher resolution and speed than the earlier light emitting diode (LED) optical mice [11]. As of 2013, the total VCSEL production is around 100 million devices per year and the price of a computer mouse 850 nm VCSEL is approaching $0.10 [11].

1.2 Organization of Thesis

The focus of this work has been to reduce the spectral width of high-speed 850 nm VCSELs in order to enable longer-reach optical interconnects. An overview of optical interconnects and state-of-the-art is presented in Chapter 2. Chapter 3 introduces the modal and dynamic characteristics of VCSELs as well as some basic properties. Chapter 4 describes the two different quasi-single mode VCSEL approaches; using a small oxide aperture or an integrated mode filter. It is followed by Chapter 5 detailing the experiments used for the dynamic characterization. The fabrication of high-speed quasi-single mode VCSELs is described in Chapter 6 and a process plan can be found in appendix A. An outlook and future directions are provided in Chapter 7. The results from the work on which this thesis is based are finally presented in the appended papers A-E which are summarized in Chapter 8.

Chapter 2

VCSELs in Optical Interconnects

The configuration of a single channel optical interconnect is shown in figure 2.1. These are often integrated into active optical cables (AOC), which are "plug-and-play" cables with electrical interfaces at both ends while the electro-optics are fully sealed. Today's optical interconnects employ GaAs-based VCSELs emitting at 850 nm. Longer wavelength GaAs-based VCSELs emitting at 980 and 1060 nm feature strained InGaAs quantum wells which favor certain high-speed properties, but 850 nm remains the standard wavelength for optical interconnects since the MMF is optimized for this wavelength [12, 13].

VCSEL-based links commonly use direct modulation and on-off keying (OOK) where the laser output is changed between two fixed levels by modulating the applied voltage. Higher level amplitude modulation formats can potentially be used to increase the spectral efficiency to enable higher speed and longer-reach transmission, but require a larger power budget [14]. Four-level pulse amplitude modulation (4PAM) has been demonstrated transmitting 12.5 Gbit/s over 600 m of fiber [15] and 60 Gbit/s back-to-back (BTB) [16].

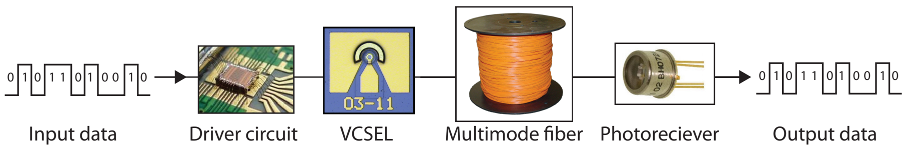

Figure 2.1: Configuration of a VCSEL-based optical interconnect link.

The work in this thesis concerns only OOK, which is likely to remain the dominant modulation format for the foreseeable future.

The MMF used in 850 nm interconnects is more expensive than SMF because of its complex refractive index profile [17]. However, because of the larger core size (50 µm compared to SMF 8 µm), MMF offers larger alignment tolerances, enabling low-cost assembly and packaging of the transmitter side of the AOC. GaAs pin photodetectors used in 850 nm optical interconnects feature a relatively large active area for efficient coupling from the large core size MMF, which translates into a larger capacitance and consequently lower bandwidth than the smaller SMF coupled photodetectors. This is equivalent to a trade-off between detector responsivity and bandwidth. The photodetector is one of the limiting factors for both reach and speed of optical interconnects, making the development of faster and more sensitive photodetectors of crucial importance.

As a rule of thumb, for transmission distances exceeding 300 m and speeds $>$10 Gbit/s, chromatic and modal fiber dispersion will significantly distort the signal [18]. If we consider this optical link to be limited by dispersion only, having a constant bit-rate-distance product, dispersion will become limiting already after 100 m at 30 Gbit/s. VCSEL-based links at $\geq$30 Gbit/s are not only limited by dispersion, but the reasoning above agrees rather well with published results, where standard high-speed VCSELs cannot transmit 30 Gbit/s over more than $\sim$100 m [19]. Quasi-single mode VCSELs with reduced spectral width may transmit over much longer distances.

2.1 Transmission Standards

Most AOCs have several channels bundled together and may have channels going in opposite directions, enabling bidirectional data transmission. In contrast to edge emitting lasers, the VCSEL vertical emission enables monolithic integrated 1D and 2D arrays of both VCSELs and photodetectors for low-cost interconnect transceivers [20]. The data is transmitted through a ribbon of MMFs with arrays of VCSELs and detectors at each end. Commercially available cables can for instance comprise 12 VCSEL links in each direction with each link operating at 12.5 Gbit/s for a aggregate capacity of 150 Gbit/s in each direction [21].

Depending on application, three different standardized data networking protocols dominate the 850 nm interconnect market; Ethernet (local area networks), Infiniband (high-performance computing, supercomputers) and Fibre Channel (storage area networks). Even though there are some differences, all support up to 10-16 Gbit/s over distances up to 300-550 m over OM4 MMF [22]. For instance 10 Gbit Ethernet (10GBASE-SR) supports 10 Gbit/s over up to 550 m, but requires a root-mean-square (RMS) spectral width of

the laser source <0.45 nm [23]. Other standards have similar requirements on RMS spectral width. Upcoming standards for 100 Gbit/s (4x25 Gbit/s) AOCs such as Ethernet 100GBASE-SR4 (25.78 Gbit/s) [24], Infiniband EDR (26 Gbit/s) [25] and Fibre Channel 32GFC (28.05 Gbit/s) [26], are all expected on the market within two years and further into the future 40 Gbit/s single channel speeds are being considered.

2.2 Data Transmission in Multimode Fiber

The launching and propagation of a modulated VCSEL signal through MMF is a complex process. To begin with the coupling of the VCSEL modes into the MMF is not a trivial problem. Depending on launch conditions such as angle, offset from fiber center and spot size, each VCSEL mode can excite several different fiber modes, referred to as mode groups. There are three main fiber-related effects that may limit the transmission distance over MMF; fiber loss, chromatic dispersion and modal dispersion. The simplest, but often not limiting, is the absorption loss during propagation in the OM4 fiber which is 2.3 dB/km. However, for commercial implementation of long-reach MMF links, it will be important to have a large received power in order to have an adequate power budget for the link, requiring quasi-single mode VCSELs with at least a few milliwatt of output power.

The separation in wavelength of the transverse modes emitted by the VCSEL causes a broadening of the signal during propagation in the MMF by chromatic dispersion, which typically amounts to around -100 ps/(nm·km) at 850 nm [23]. In addition, the different modes in the fiber have different propagation constants, giving rise to modal dispersion. During modulation, the relative optical power in the VCSEL modes fluctuate by mode competition, even when the total output power is constant. The fluctuating modes cause a random fluctuation in the effects of modal dispersion and possible mode-selective losses and coupling, collectively referred to as mode partition noise. In highly multimode VCSEL links the mode partition noise is reduced by the averaging over many modes, but lasers with a few modes can suffer greatly. Due to the absence of other modes, single mode lasers do not experience any significant mode partition noise.

The newer OM3 and OM4 MMFs have optimized graded index profiles in order to minimize the modal dispersion, making chromatic dispersion the dominating effect [27]. There is ongoing research on developing new MMF fiber with even higher bandwidth due to lower chromatic and modal dispersion [27, 28]. In particular, by optimizing the MMF refractive index profile, modal and chromatic dispersion can compensate each other, in effect partly canceling out the effect of dispersion.

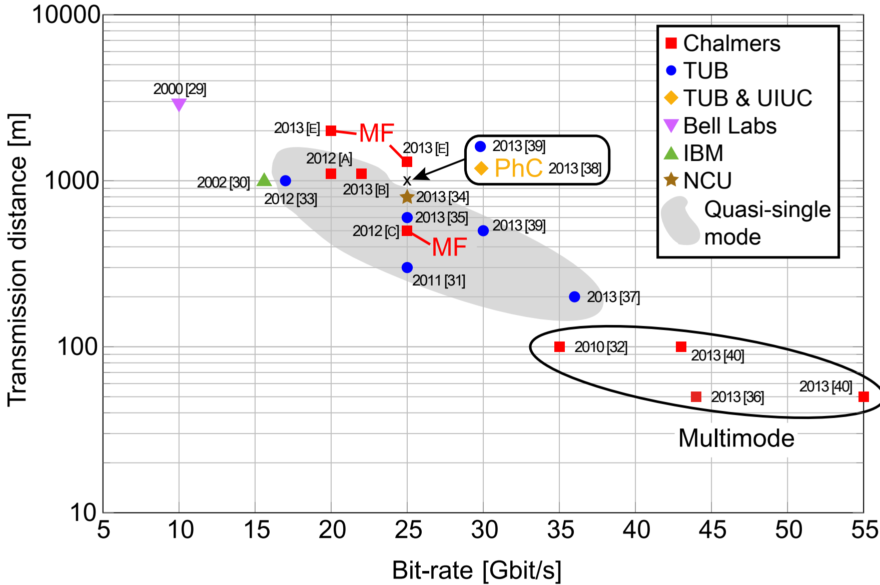

Figure 2.2: State-of-the-art high-speed long-distance transmission using 850 nm VCSELs and multimode fiber. All VCSELs outside of the multimode or quasi-single mode areas are single mode, except the IBM VCSEL which is a large aperture multimode VCSEL, but with a RMS spectral width of 0.44 nm. All devices except the photonics crystal (PhC) are oxide confined and only the mode filter (MF) and PhC VCSELs have special mode-selective structures. All links perform at bit-error-rate $<10^{-12}$ except the IBM link where only open eyes are shown. (TUB=Technical University Berlin, UIUC=University of Illinois at Urbana-Champaign, NCU=National Central University.) [29–40], and papers A, B, C and E.

2.3 State-of-the-Art

Giaretta *et al.* [29] and Pepeljugoski *et al.* [30] demonstrated already in 2000 and 2002, respectively, that 850 nm VCSEL links at >10 Gbit/s over >1 km of MMF are feasible by using low spectral-width VCSELs. As a matter of fact, Giaretta still holds the record for the highest *published* bit-rate-distance product with 28.2 Gbit·km/s (10 Gbit/s over 2820 m) using a single mode VCSEL. Since then the bandwidth of oxide-confined 850 nm VCSELs has seen a large increase, recently reaching a record 28 GHz in 2012 [41]. This development has sparked an interest in extending the reach of high-speed (>20 Gbit/s) links. The 2011 paper [31] by Fiol et al from Technische Universität Berlin

(TUB) demonstrating 25 Gbit/s over 300 m of OM3 fiber started the race. Only two years later researchers from Chalmers University of Technology, TUB and University of Illinois at Urbana-Champaign (UIUC) have demonstrated >20 Gbit/s links over ≥1 km of MMF [38, 39] and papers A and B, see figure 2.2. This has been possible by reducing the spectral width of recently developed high-speed VCSELs.

The most common approach is to use a small oxide aperture of ∼3 µm as used in [33, 35, 39] and papers A and B. Philip Moser *et al.* from TUB have show that these small-aperture devices can transmit data at record-low energy consumption [35, 42]. Even though small oxide aperture high-speed VCSELs do not have the highest wall-plug efficiency (<20% compared to ≥30% for larger oxide apertures), they have excellent high-speed properties at low bias currents because of the small active and modal volumes (see section 3.5). This becomes important as datacenters consume vast amounts of energy; a new Facebook datacenter in Luleå, Sweden, is projected to consume 1 TWh per year, equivalent to the city of Västerås with 140 000 inhabitants [43]. Reducing the power consumption of optical interconnects is important even though they only constitute a smaller part of the total datacenter energy consumption [44]. Furthermore, the VCSEL usually consumes just a small fraction of the total interconnect power [42]. However, recent results have shown that energy-efficient CMOS driver and receiver circuits can be fabricated, increasing the VCSEL's share of the interconnect's power consumption to 30-40% [45], thus making more energy-efficient VCSELs an important research direction.

The optical guiding can also be modified by etching a photonic crystal on high-speed VCSELs as demonstrated by Tan *et al.* from UIUC, enabling transmission at 25 Gbit/s over 1000 m [38]. Photonic crystal VCSELs can have excellent spectral properties and low resistance, but increased scattering loss reduces the output power. The technique of using a surface relief mode filter to reduce the spectral width of VCSELs is applied in papers C and D, enabling transmission at 25 Gbit/s over 500 m. Very recent results from a new single mode mode filter VCSEL from Chalmers enabled transmission of 25 Gbit/s over 1300 m of OM4 fiber and 20 Gbit/s over 2000 m, setting a new bit-rate-distance product record of 40 Gbit·km/s. These results are yet to be published, but can be found in paper E. The mode filter technique allows for a larger oxide aperture with potentially lower differential resistance and higher output power to compensate for propagation loss in long-reach links. Shi *et al.* from National Central University, Taiwan, used a combination of mode filtering by Zn-diffusion and and small oxide relief (where the oxidized layer is completely removed for low capacitance) to achieve quasi-single mode operation, enabling 25 Gbit/s over 800 m [34].

During the last year, several record-high transmission speeds for directly modulated 850 nm VCSELs have been reported by Westbergh *et al.* from

Chalmers, with 47 Gbit/s and 57 Gbit/s back-to-back (BTB) [36, 40]. These devices are multimode with wide optical spectra, but could nevertheless transmit 43 and 55 Gbit/s over 100 and 50 m of MMF respectively [40].

Chapter 3

VCSEL Design and Characteristics

As the name indicates, vertical-cavity surface-emitting lasers (VCSELs) emit light normal to the surface by lasing in a vertical cavity, see figure 3.1a. The cavity is formed by two highly (~99%) reflective mirrors, usually distributed Bragg reflectors (DBRs), with a forward biased pn-junction inbetween providing optical gain. In contrast to the VCSEL, the earlier developed edge-emitting Fabry Perot laser has a horizontal resonator with cleaved semiconductor-air facets acting as mirrors, see figure 3.1b. This means that the wafer must be cleaved to enable testing and screening, while VCSELs may be tested on-wafer during production and integrated into 2D arrays. VCSELs are sometimes referred to as micro-cavity lasers and have several additional advantages because of the small cavity size, such as low threshold current and high-speed properties superior to edge-emitting lasers.

3.1 VCSEL Cavity

The longitudinal resonance of the VCSEL cavity is set by the phase condition, that the optical field must repeat itself after one round-trip in the cavity, meaning that twice the optical length Ln_{eff} of the cavity must equal an integer number m of wavelengths λ_0 according to

$$2Ln_{eff} = m\lambda_0 \Rightarrow \lambda_0 = \frac{2Ln_{eff}}{m}. \tag{3.1}$$

Because of the short cavity length, the VCSEL cavity only has one longitudinal mode within the gain spectrum making the device inherently single longitudinal mode (though usually not single transverse mode), see figure 3.2.

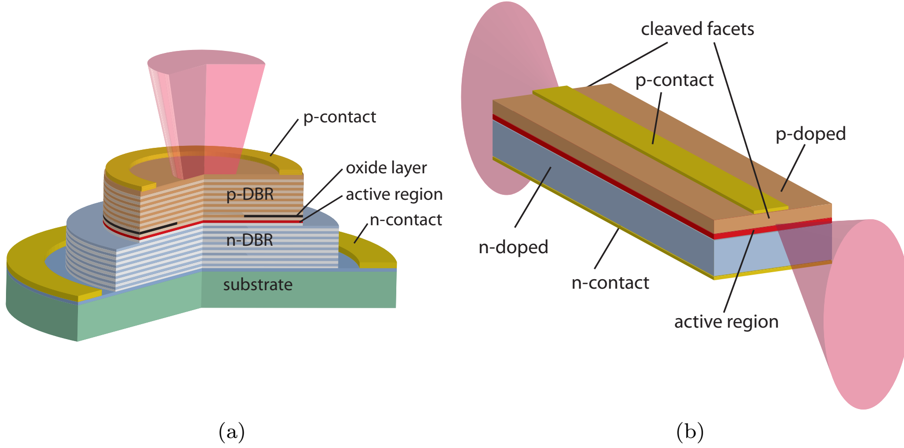

Figure 3.1: (a) Cut-through VCSEL sketch. (b) Schematic figure of an edge emitting stripe laser with elliptical emission beams.

The distributed Bragg reflector (DBR) mirrors comprise a stack of alternating high and low refractive index material where the light is partially reflected at each interface. If the optical thickness of each layer equals a quarter wavelength ($\lambda/4n$), this wavelength will experience the Bragg condition, meaning that all reflections add up in phase leading to a large reflection, see figure 3.2a. The peak reflectivity depends on the refractive index difference ($n_2 - n_1$) and the number of DBR pairs, while the width of the spectrum mainly depends on the index difference.

DBRs are commonly fabricated from either dielectric or epitaxial material systems. Dielectric DBRs may achieve a high reflectivity with $<$10 pairs due to the high index contrast (e.g. TiO_2/SiO_2 with $n_2 - n_1 = 0.90$ at 850 nm [46]), while epitaxial DBRs need ~20-30 pairs because of the lower index contrast (e.g. $Al_{0.12}Ga_{0.90}As/Al_{0.90}Ga_{0.10}As$ with $n_2 - n_1 = 0.46$ [47]). On the other hand epitaxial DBRs can be doped and often function as current spreaders to achieve a uniform injection into the active region. For the mirror where no emission is required, hybrid DBRs may be used where the DBR's final layer of gold or copper increases reflectivity and may also function as a heat sink. GaAs-based VCSEL designs commonly feature epitaxial DBRs from the mature AlGaAs material system. Longer wavelength VCSELs with InP-based active regions emitting at 1.3 and 1.55 µm usually have at least one dielectric DBR or wafer fused AlGaAs DBRs, since InP-based DBRs have a very low refractive index contrast [48, 49].

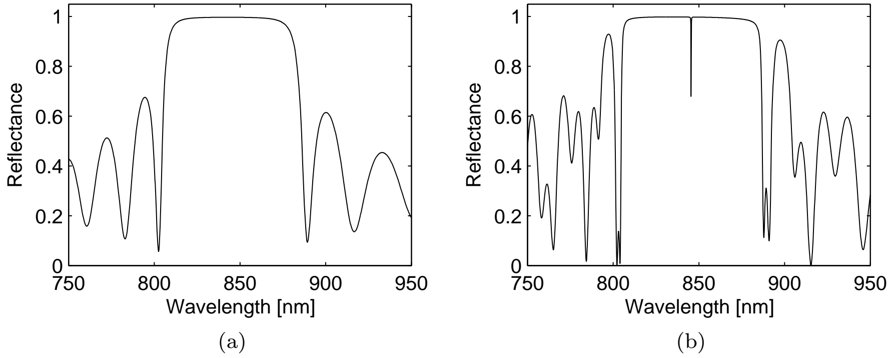

Figure 3.2: Calculated reflectivity spectra for (a) the VCSEL top DBR with 23 pairs of $Al_{0.90}Ga_{0.10}As/Al_{0.12}Ga_{0.88}As$ and (b) the full VCSEL cavity. The single narrow longitudinal resonance is seen at 845 nm.

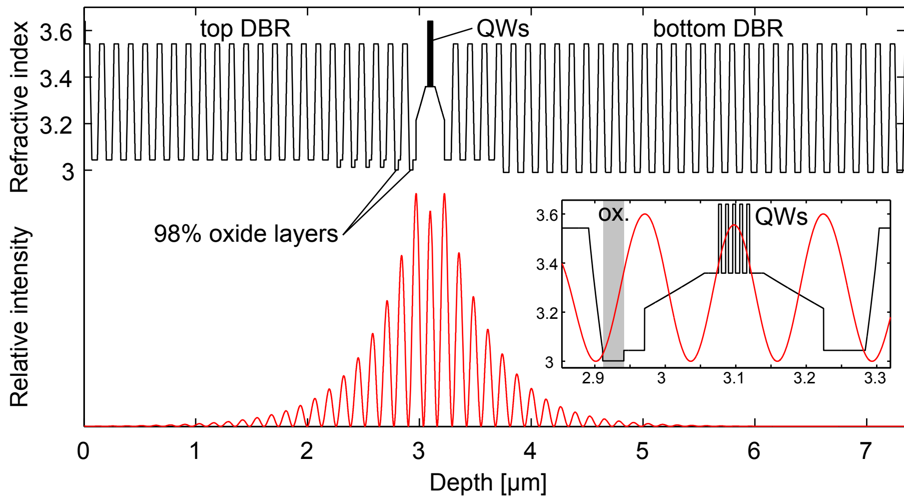

Figure 3.3: Refractive index profile and the simulated standing wave of the optical field inside a VCSEL cavity. The inset shows the overlap of the standing wave with the quantum wells (QWs) and the nearest oxide layer (ox.). The substrate is to the right.

3.2 Active Region

The active region provides the optical gain. During lasing the modal gain must balance the optical losses according to

$$g_{th} = \frac{1}{\Gamma}\left(\alpha_i + \frac{1}{2L}\ln\frac{1}{R_1 R_2}\right) \tag{3.2}$$

where g_{th} is the threshold gain, Γ the optical confinement factor representing the portion of the standing wave that overlaps the quantum wells, α_i the internal optical loss (mainly due to free carrier absorption and diffraction loss), L the effective length of the cavity and R_1 and R_2 are the top and bottom mirror reflectances.

In semiconductor lasers the optical gain by stimulated emission is achieved by injecting carriers into a forward biased pn-junction. Electrons and holes accumulate in the conduction and valence band respectively which under high enough injection gives rise to a population inversion and thereby optical gain. The first semiconductor laser demonstrated in 1962 had an active region consisting of a GaAs homojunction and could only operate in pulsed mode at 77 K because of the high band-to-band absorption [50]. Today the active region usually consists of a pin-heterojunction with quantum wells situated in the lower-bandgap intrinsic layer. The quantum wells trap the carriers, providing a high carrier density and a good spatial overlap between the electron and hole wave functions. Since the stimulated emission process is related to the optical field strength, the quantum wells are placed at an antinode of the optical field to achieve a high gain, see figure 3.3. State-of-the-art high-speed VCSELs now use strained InGaAs quantum wells which reduces the density of states, meaning that fewer carriers are required to reach a certain gain (i.e. a larger differential gain) [51].

3.3 Optical and Electrical Confinement

The DBRs confine the optical field in the longitudinal direction (figure 3.3), but it must also be confined in the transverse direction. Furthermore, the electrical current must be confined to pump only active material overlapping with the transverse optical modes. In most VCSEL designs the electrical and optical confinement originate from the same feature. The first VCSELs consisted of an etched air post mesa, see figure 3.4a, with the refractive index step from semiconductor to air providing index guiding, confining the optical field in the transverse direction. Although simple, this design has several issues such as poor thermal management, large scattering losses from rough sidewalls and trouble with placing large enough top contacts for low resistance, while avoiding absorption losses from the metal. A further development is the buried

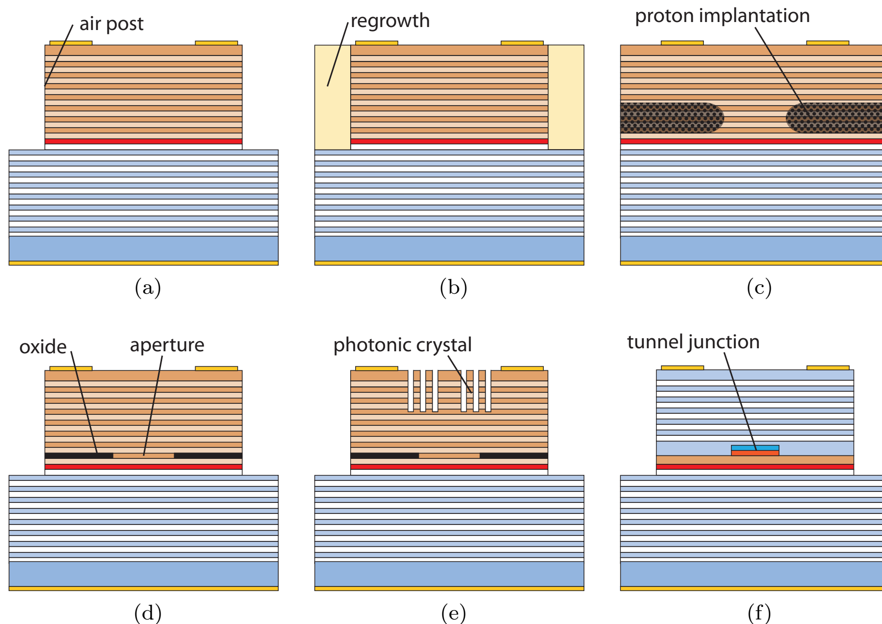

Figure 3.4: Different electrical and optical confinement methods, (a) etched air post, (b) regrown mesa, (c) proton implantation, (d) oxide aperture, (e) photonic crystal and (f) buried tunnel-junction.

heterostructure VCSEL seen in figure 3.4b. By regrowing semi-insulating semiconductor material around the etched mesa, problems with thermal resistance and losses are avoided, but the regrowth process is very challenging. The first commercial VCSELs instead used proton implantation, see in figure 3.4c. Protons are implanted deep into the top DBR forming a current aperture, but no significant direct index step for transverse optical confinement. However, as the center of the waveguide heats up during operation, the refractive index increases by the thermo-optic effect, creating an index step. This effect (referred to as thermal lensing) confines the optical field, but also leads to unstable modal properties depending on the bias current. Scattering of the protons during implantation due to the large penetration depth into the top DBR makes it difficult to fabricate small aperture devices.

Stable modal properties are obtained by including a sufficiently large built-in index step to make thermal lensing, gain guiding and plasma effect (decreasing refractive index with increased carrier concentration) small in comparison. One approach is to use a selectively oxidized layer forming an oxide aperture,

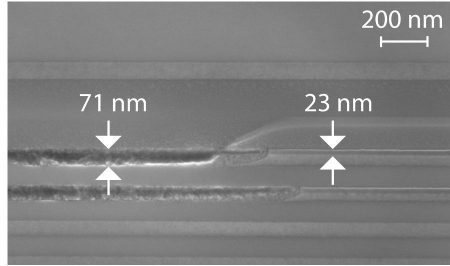

Figure 3.5: Scanning electron microscope (SEM) image of a double oxide aperture oxidized from the left with a 23 nm $Al_{0.98}Ga_{0.02}As$ layer showing the vertical oxidation of the $Al_{0.90}Ga_{0.10}A$ layer below.

see figure 3.4d. A high Al-content layer (usually $Al_{0.98}Ga_{0.02}As$) is positioned close to the active region. When the etched mesa side is exposed to hot water vapor this layer will oxidize to form an insulating oxide with reduced refractive index, in effect creating a current aperture as well as providing transverse optical guiding. The oxidation rate is strongly dependent on the Al-content and the highest Al-content layer will form the smallest oxide aperture [52]. To avoid too large index guiding, the oxide layer is usually positioned close to a node of the optical field [53], see figure 3.3. Multiple oxide layers may be used in order to reduce mesa capacitance to mitigate parasitic bandwidth impairments [54]. It has also been seen that the $Al_{0.90}Ga_{0.10}As$ layer closest to the 98% layer can oxidize vertically from the 98% layer during oxidation. This effectively increases the thickness of the oxide layer from the designed 20-30 nm to 70 nm, see figure 3.5. This increases the index guiding, but also leads to a reduced capacitance [55]. Oxide confinement is used in this work and is the most commonly used confinement scheme in GaAs-based VCSELs today.

Decoupling of the electrical and optical confinement, in order to tailor the optical properties of the VCSEL waveguide, can be achieved by etching a 2D photonic crystal into the top DBR of an oxide-confined or proton implanted VCSEL, see figure 3.4e. In addition to increased design and processing complexity, the photonic crystal structure increases optical scattering losses, leading to lower output power and larger threshold current [11]. For long-wavelength InP-based VCSELs emitting at 1.3 and 1.55 µm, a buried tunnel junction is used for electrical and optical confinement since no high-quality oxide exists in this material system, see figure 3.4f. This technique is not commonly used for GaAs-based VCSELs because of the complex growth and processing and the excellent properties of oxide-confined VCSELs.

3.4 Spectral Characteristics

VCSELs in general have a short effective cavity length on the order of a couple of wavelengths, and high-speed VCSELs in particular usually have the shortest cavity possible of 0.5λ or 1.5λ since this enhances the modulation bandwidth. Only one longitudinal mode falls within the gain spectrum and may lase because of the short cavity. However, due to the large lateral dimensions the VCSEL cavity may support several transverse modes. The spectral characteristics of the VCSEL can be analytically investigated using an effective index method [56], where the radial refractive index step is modeled as a parabolic refractive index profile according to

$$n^2(r) = \begin{cases} n_c^2(1 - 2\Delta r^2/a^2) & , r \leq a \\ n_s^2 = \text{const} & , r > a \end{cases} \quad \text{with} \quad \Delta = \frac{n_c^2 - n_s^2}{2n_c^2} \approx \frac{n_c - n_s}{n_c} \tag{3.3}$$

where r is the radial distance, a the radius of the oxide aperture, n_c the core effective refractive index and n_s the effective index of the surrounding oxide region. It should be noted here that although equation 3.3, strictly speaking, describes a thermally guided VCSEL (e.g. an ion implanted VCSEL), it may be used to approximate an oxide confined VCSEL [11, 56]. The beauty is that this derivation yields analytical expressions, useful for understanding the VCSEL modal properties. By solving the wave equation in this circular symmetric structure, the near-field intensity of the transverse modes becomes

$$S_{lp}(r,\Phi) \propto |E_{lp}(r,\Phi)|^2 \propto \left(\frac{2r^2}{\omega_0^2}\right)^l \left[L_{p-1}^{(l)}\left(\frac{2r^2}{\omega_0^2}\right)\right]^2 \begin{Bmatrix} cos^2(l\Phi) \\ sin^2(l\Phi) \end{Bmatrix} \exp\left(\frac{-2r^2}{\omega_0^2}\right) \tag{3.4}$$

where E is the optical field strength, ω_0 the spot radius, L_{p-1}^l the lth generalized Laguerre polynomial of order $(p-1)$, and Φ the azimuthal angle. The modes are referred to as linearly polarized LP_{lp} modes with intensity distribution as shown in figure 3.6. For $l > 0$ the *sin* and *cos* factors represent two different orthogonal states rotated $90°/l$ with respect to each other. Furthermore, every mode has two different polarization states with the electric field oscillating perpendicular to the propagation direction. The fundamental mode LP_{01} has a Gaussian intensity distribution and two different polarization states, while the higher order modes with $l > 0$ have four polarization states per LP_{lp} mode. The wavelength λ_{lp} of mode LP_{lp} differs the fundamental longitudinal mode λ_0 as [56]

$$\lambda_{lp} = \lambda_0 \left[1 - (2p + l - 1)\frac{\sqrt{\Delta}}{\sqrt{2}\pi}\frac{\lambda_0}{n_c a}\right], \tag{3.5}$$

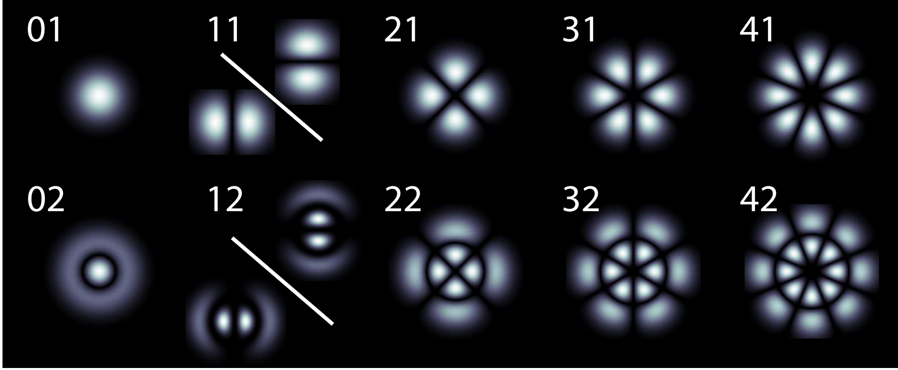

Figure 3.6: Transverse intensity distributions of the lowest order LP_{lp} modes plotted from equation 3.4. LP_{11} and LP_{12} exemplify the rotated polarization states (*cos* and *sin*) which exists for $l > 0$.

which shows that the modes with the same mode index $m = 2p+l-1$ have the same emission wavelength. The order and spacing of the modes agree well with the measured spectrum and near-field images in paper D. From equation 3.5 the mode spacing between adjacent mode index groups is

$$\Delta\lambda = |\lambda_m - \lambda_{m+1}| = \frac{\sqrt{\Delta}}{\sqrt{2}\pi} \frac{\lambda_0^2}{n_c a} \propto \frac{\sqrt{\Delta}}{D_{ox}}, \tag{3.6}$$

where $D_{ox} = 2a$ is the oxide aperture diameter. Equation 3.6 can be used to experimentally estimate the refractive index step Δ by measuring $\lambda_{01} - \lambda_{11}$ in the optical spectrum. The number of guided modes is determined from the normalized frequency V

$$V = \frac{2\pi a}{\lambda} \sqrt{n_c^2 - n_s^2}. \tag{3.7}$$

Just like an step-index SMF, the waveguide is single mode if $V < 2.405$ [57]. For a large V the number of guided transverse modes can be estimated by

$$M = \frac{V^2}{4}. \tag{3.8}$$

In reality, these equations are merely approximate due to the complicated interplay between guiding, gain and loss in a biased VCSEL.

In order to quantify and compare different VCSELs the communication standards usually specify a maximum root-mean-square (RMS) spectral width for a VCSEL, which is calculated according to

$$\Delta\lambda_{RMS} = \sqrt{\sum_{i=1}^{n} \frac{P_i}{P_{tot}} \left(\lambda_i - \langle\lambda\rangle\right)^2} \;, \quad \langle\lambda\rangle = \sum_{i=1}^{n} \frac{P_i}{P_{tot}} \lambda_i \;, \quad P_{tot} = \sum_{i=1}^{n} P_i \quad (3.9)$$

where n is the number of data points of the measured spectrum, P_i is the power of point i at λ_i and P_{tot} is the total optical power. Since the VCSEL spectrum consists of few peaks with an asymmetric envelope, the use of the RMS width to quantify VCSEL spectral width can be questioned, especially for quasi-single mode lasers. It is, however, a simple measurement and it is used to set VCSEL requirements in all transmission standards.

3.5 Dynamic Properties

The bandwidth of any semiconductor laser is limited by damping of the intrinsic carrier-photon interaction, extrinsic parasitics and thermal effects. From the rate equations the small signal transfer function of a semiconductor laser is found to be that of a second order damped system described by a resonance frequency (f_r) and a damping factor (γ). Since VCSELs have multiple lasing modes, a strict rate equation analysis should involve one rate equation for each mode. It has, however, been shown by both experiment and simulation that oxide-confined VCSELs are well described by single mode rate equations because of the tight overlap of the modes due to the index guiding [58]. By introducing an extra pole for the parasitic effects with cut-off frequency f_p, the three-pole VCSEL transfer function is [59]

$$H(f) = \text{const} \cdot \frac{f_r^2}{f_r^2 - f^2 + j\frac{f}{2\pi}\gamma} \cdot \frac{1}{1 + j\frac{f}{f_p}}. \quad (3.10)$$

The D-factor describes how fast the resonance frequency increases with bias current I above the threshold current I_{th}

$$f_r \equiv D \cdot \sqrt{I - I_{th}} \quad \text{with} \quad D = \frac{1}{2\pi}\sqrt{\frac{\eta_i v_g}{qV_p} \cdot \frac{\partial g/\partial n}{\chi}}, \quad (3.11)$$

where η_i is the internal quantum efficiency, v_g the group velocity, q the elementary charge, V_p the mode volume, $\partial g/\partial n$ the differential gain and χ the transport factor. From equation 3.11 it is seen that the small mode volume enables a VCSEL to reach high resonance frequencies at low bias currents for energy-efficient modulation. A large differential gain from strained quantum wells and high internal quantum efficiency are also beneficial. The VCSEL resonance frequency will keep increasing with bias current until the self-heating

leads to thermal effects that decreases η_i and $\partial g/\partial n$, as well as increases I_{th} [60]. Self-heating can be reduced by for instance lower device resistance, higher quantum efficiency and lower thermal resistance to efficiently transport away generated heat. This is important for future high-speed VCSELs, especially for commercial devices which should be capable of operating in an ambient temperature of up to 85°C.

The intrinsic damping of the VCSEL increases with resonance frequency squared as

$$\gamma = Kf_r^2 + \gamma_0 \quad \text{with} \qquad K = 4\pi^2 \left(\tau_p + \frac{\varepsilon\chi}{v_g \frac{\partial g}{\partial n}} \right), \tag{3.12}$$

where γ_0 is the damping factor offset, τ_p the photon lifetime and ε the gain compression factor. The K-factor should be small for a large intrinsic bandwidth. However, a too low K-factor can result in low damping of the relaxation oscillations during large signal modulation and consequently increased overshoot and noise during data transmission. The VCSEL bandwidth can be significantly improved by optimizing the photon lifetime for low damping. By a shallow (<60 nm) etch into the top DBR, the mirror reflectivity can be continuously varied over a large range, allowing a post-process setting of the photon lifetime [61]. The change in mirror reflectivity will also affect static properties such as threshold current, slope efficiency and internal absorption rate.

By virtue of strained quantum wells for increased differential gain [62] and optimized photon lifetimes for low damping [61], recent high-speed VCSELs have high intrinsic bandwidths in excess of 30 GHz. The VCSEL bandwidth is therefore limited by the parasitic roll-over from device capacitances and resistances. Part of the resistance originates from transport through the DBR mirrors, but the largest part is due to funneling current through the narrow oxide aperture [54]. DBR resistance can be decreased by employing innovative modulation doping and grading of the DBR interfaces [36]. There is, however, a trade-off between high doping and low free-carrier absorption. The capacitance also has one major and one minor contribution; the mesa capacitance over the oxide layers and active region, and secondly the bondpad capacitance. Bondpad capacitance is kept low by using a thick layer of benzocyclobutene (BCB) with a low dielectric constant to planarize the VCSEL mesa and separate the bondpads. The n-doped GaAs contact layer is also etched away underneath the p-bondpad, leaving only the semi-insulating substrate, in order to further reduce bondpad capacitance. To reduce mesa capacitance, recent high-speed oxide-confined VCSEL designs use multiple oxide apertures [61].

Chapter 4

Quasi-Single Mode VCSELs

For a VCSEL to be referred to as single mode, a side-mode suppression ratio (SMSR) larger than 30 dB is typically required. If nothing else is specified, *single mode* usually refers to a VCSEL lasing in the fundamental LP_{01} mode, which has two different polarizations. Single polarization emission can be achieved by introducing some anisotropy in the waveguide for instance by using gratings [63]. Single mode VCSELs have been extensively researched since the beginning of VCSEL development. It is essential for long-wavelength (1.3 and 1.55 µm) communication VCSELs and many sensing applications such as gas sensing where a single mode laser source is needed [64]. However, most applications poise complicated demands on the VCSEL leading to a trade-off between output power, high-speed properties and emission spectrum. As previously discussed in figure 2.2, almost all of the reported highest bit-rate-distance product 850 nm VCSEL links today use single mode or quasi-single mode VCSELs. The term *quasi-single* mode does not have a clear definition, other than being a VCSEL that is *almost* single mode. The term is used in this thesis to refer to VCSELs with an SMSR of ∼15-20 dB.

There are several designs aimed at achieving single mode or low-spectral width of 850 nm GaAs-based VCSELs, but all work in essentially two different ways; an inherently single mode waveguide, or a mode selective loss. The former includes photonic crystal VCSELs and basically any device with a narrow enough transverse aperture and sufficiently small index step. Mode selective losses can be implemented by for instance metal apertures, extended cavities and shallow surface reliefs [65]. There are also more complex VCSEL designs with non-epitaxial structures such as using a curved external mirror which has achieved 15 mW of single mode power [66]. This thesis concerns two of

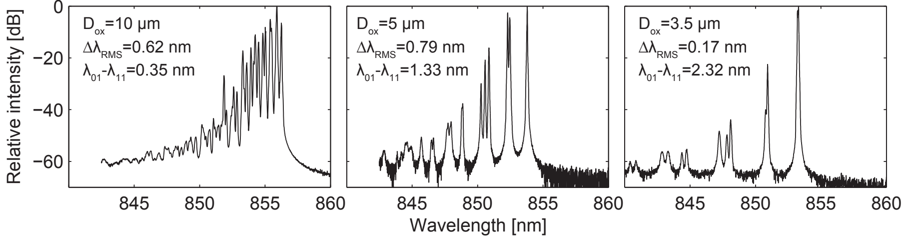

Figure 4.1: VCSEL spectra for decreasing oxide aperture with values for RMS spectral width and the mode spacing between the fundamental and first higher order mode ($\lambda_{01} - \lambda_{11}$). The VCSELs are biased about halfway to their respective thermal roll-over.

the most promising approaches to simultaneously achieve excellent high-speed properties and low spectral width, by either using a small oxide aperture or an integrated surface relief mode filter.

4.1 Small Oxide Aperture

A large oxide aperture and strong index guiding results in a large V and many guided modes, see equation 3.7 and figure 4.1. Hence, reducing the oxide aperture diameter to reduce the number of guided modes could be believed to reduce the spectral width. However, doing so will lead to a larger mode spacing (according to equation 3.6), which comes in squared when calculating the RMS width (equation 3.9). In general, large aperture devices will have a relatively narrow spectral width because the mode spacing is small, but the numerous modes will lead to significant modal dispersion during long-reach transmission. Shrinking the oxide aperture reduces the number of modes, but does not decrease the spectral width because of the increased mode spacing, in effect reducing modal dispersion at the cost of increased chromatic dispersion. In order to simultaneously reduce the effects of chromatic and modal fiber dispersion and reach a low RMS width, a single mode or quasi-single mode VCSEL is required. This is illustrated in figure 4.1.

A quasi-single mode VCSEL is obtained first at an oxide aperture size of ~3.5 µm for high-speed VCSELs, while single mode operation requires even smaller oxide aperture of just ~2 µm. For lower index guiding, such as ion implantation or oxide-confined VCSELs with only one thin oxide layer, apertures around 4-5 µm may yield single mode emission. For instance a high single mode power of 4.8 mW has been obtained using an 3.5 µm single oxide aperture VCSEL [67]. Even though small aperture devices have excellent spectral

properties, there are several drawbacks of such a small device aperture. The output power is relatively small, in general being limited to 1-2 mW, giving a limited power budget for long-reach links. A very small oxide aperture can also enhance diffraction losses, leading to higher threshold current and lower output power. Funneling the bias current through the small aperture leads to an increase in differential resistance from $<100\ \Omega$ for 7 µm devices, to 200-300 Ω for a small-oxide device. The large impedance mismatch between the VCSEL and the driver leads to large microwave reflections and inefficient transfer of the modulation energy.

Although smaller devices operate at smaller currents, the current density (bias current divided by oxide aperture area) is increased compared to large devices. The industry standard for reliable operation is 10 kA/cm^2 [68], while the reported small-oxide VCSELs for long-reach transmission operate at 20-35 kA/cm^2 [35, 39] and paper A. These high current densities may shorten the device lifetime, leading to premature device failure. On the other hand, smaller oxide aperture VCSELs seem to handle higher current densities better [68], likely because of the larger perimeter relative to the active area. In a recent reliability study, 50 high-speed VCSELs with 6 µm oxide-aperture were biased at 5 mA (18 kA/cm^2) at 95°C for 6000 h without any failures [69], indicating that relatively small oxide aperture devices can operate reliably at elevated current densities. However, the reliability of even smaller oxide aperture (2-4 µm) high-speed VCSELs with InGaAs quantum wells and multiple oxide apertures has still not been thoroughly evaluated (to my best knowledge).

The fabrication of small-oxide aperture VCSELs is straightforward with no extra processing steps, but requires a reproducible and uniform oxidation process. Since the oxidation rate is exponentially dependent on the temperature, a temperature variation across the wafer below 0.5° is required. This can, however, be managed by a well calibrated fabrication process, and small-oxide apertures devices are actually the highest-volume production VCSEL type since they are used in optical computer mice [11]. It should be noted that the lifetime requirements on VCSELs for communication are likely much stricter. In addition, optical computer mice VCSELs usually have single oxide layers and operate at a smaller current density (1.5 mA for a 4 µm device, 12 kA/cm^2) than what is necessary for high-speed operation [11].

The small-oxide aperture approach is explored in papers A and B.

4.2 Surface Relief Mode Filter

Instead of altering the guiding of the waveguide, a mode-selective loss can be used to suppress higher order modes. One of the things that distinguish the different transverse modes in a VCSEL, is their different spatial intensity distributions, see in figure 4.2a. Hence, by introducing a spatially varying loss,

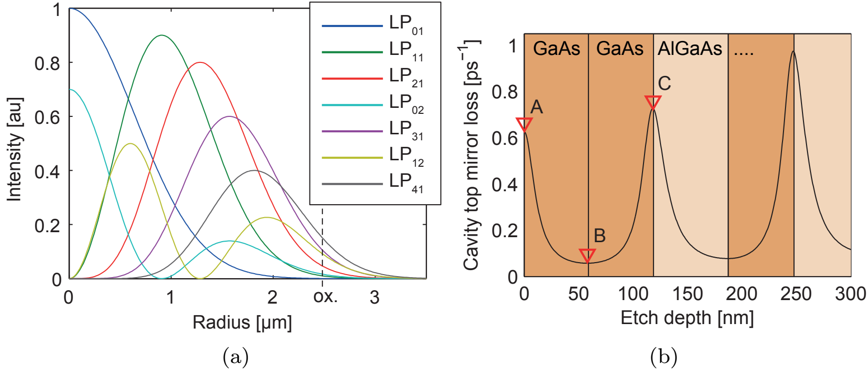

(a) (b)

Figure 4.2: (a) Radial intensity distributions of the 7 lowest order transverse modes in a 5 µm oxide aperture VCSEL (from equation 3.4, ox.=oxide aperture edge). (b) Calculated top mirror loss rate as a function of etch depth.

the threshold of the higher order modes can be made larger than that of the fundamental mode. The top mirror loss can be greatly varied by etching into the topmost layer of the top DBR, see figure 4.2b. Because of the periodic DBR structure, etching away one quarter wavelength layer will change the phase of the semiconductor-air reflection, in essence modifying the top mirror reflectivity. For a DBR with an initial anti-phase top reflection (point A in figure 4.2b), etching away the top 59 nm of GaAs results in an in-phase reflection (point B in figure 4.2b) and lower mirror loss (corresponding to higher mirror reflectivity). Etching a quarter wavelength deep hole into the top anti-phase layer, lowers the mirror loss in the center of the waveguide, lowering the threshold for the fundamental mode which has the largest overlap with the etched region, see figure 4.3b. The etched hole, called an inveted surface relief, functions as an integrated mode filter.

Most early mode filter VCSELs featured an initial in-phase top reflection, equivalent to beginning at point B (figure 4.2b) and etching a donut-shaped pattern to point C, see figure 4.3a. The drawback of this design is that it requires a very precise etch to point C. For an inverted surface relief, the high precision of epitaxial growth is instead used to grow the material to an anti-phase reflection, reducing the precision requirements for the shallow etch. For optimal mode selectivity the mode filter should have a diameter equal to half the oxide aperture and be centered in the oxide aperture [70].

Mode filtering by shallow surface etching was first demonstrated by Dowd *et al.* in 1997, achieving single mode emission for large aperture implanted VCSELs and a spectral narrowing for oxide-confined VCSELs [71]. The technique was further developed mainly by Chalmers University of Technology

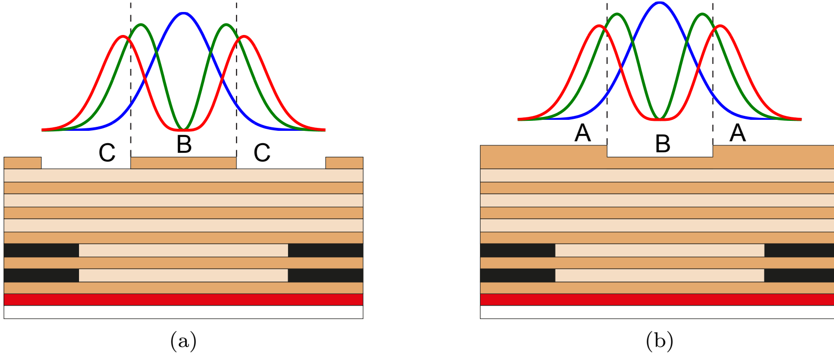

Figure 4.3: Schematic figure of surface relief techniques illustrating the oxide aperture and the overlap of the three lowest-order modes (LP_{01}, LP_{11} and LP_{21}) for (a) donut shaped surface relief etched from B to C and (b) inverted surface relief etched from A to B in 4.2b.

[63, 70, 72] and Universität Ulm [73–75] from the late 1990's. The mode filtering technique has successfully achieved single mode VCSELs with output powers exceeding 6 mW [72, 75]. For applications such as gas sensing, where a single polarization is desired, a subwavelength grating surface relief can be used to achieve polarization stable single mode emission [63, 74]. The surface relief method has also been applied to other material systems, for instance AlGaSb VCSELs emitting at 2.35 µm [76]. High-speed VCSEL with inverted surface reliefs are investigated in papers C, D and E.

4.2.1 Effects on Static Characteristics

Since the shallow surface etching affects the top DBR reflectivity, the threshold current and slope efficiency are also affected. For an initial anti-phase top DBR, the inverted surface relief etching increases the overall top mirror reflectivity, in effect lowering the threshold current and slope efficiency. A large reflectivity also leads to a longer photon lifetime, leading to an increased internal absorption rate, stronger damping of the modulation response and a consequently lower bandwidth [61]. A shorter photon lifetime for lower damping requires a larger overall loss, but a successful mode discrimination still requires a large loss difference. This seems possible by for instance using fewer mirror pairs, as seen in figure 4.2b. The top mirror loss is in general increased for fewer mirror pairs and the maximum loss difference also increases.

Chapter 5

High-Speed Characterization

Proper characterization of the VCSEL's performance in fiber optical links requires carefully aligned and calibrated measurement systems.

5.1 Small-Signal Modulation Response

The equations governing the small-signal dynamics discussed in chapter 3 enables the studying of the VCSEL dynamics. By measuring the small-signal modulation response (S_{21}) of the VCSEL and fitting equations 3.10 to 3.12 important parameters can be extracted. A small sinusoidal signal from a network analyzer is combined with the bias current through a bias-T and fed to the VCSEL through a high-frequency RF probe, see figure 5.1. The output light is focused by an anti-reflection coated lens system on an angled facet short fiber, which minimizes optical feedback from the measurement setup. A photodetector is used to detect the signal which is fed back to the network analyzer. The measured data is corrected for the photodetector response and probe insertion loss. In addition to S_{21}, the reflection coefficient (S_{11}) may be measured to fit an equivalent circuit in order to analyze the parasitic resistances and capacitances of the device [54].

5.2 Large-Signal Modulation and Data Transmission

A realistic system test is necessary to fully characterize the VCSEL performance in a datacom link. This is performed by setting up a fiber optical link and transmitting a bit sequence through it. By comparing the sent and received bits, the bit-error-rate (BER) is measured. The measurement setup

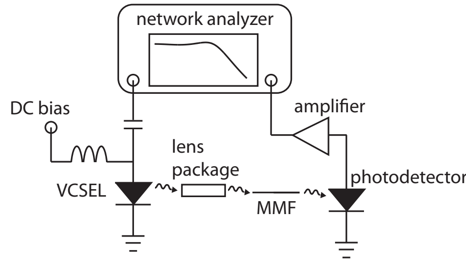

Figure 5.1: The small-signal measurement setup.

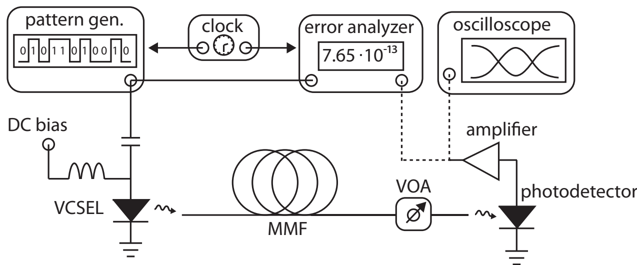

Figure 5.2: The BER measurement setup. (VOA = variable optical attenuator)

is seen in figure 5.2. A pattern generator generates a pseudorandom binary sequence (PRBS) of length $2^7 - 1 (= 127)$ bits which is combined with the DC bias through a bias-T and fed to the VCSEL using a high-frequency RF probe. The output light is butt-coupled to a MMF which is either short (≤ 2 m) for back-to-back measurements (BTB) or longer for distance transmission. An optical attenuator is placed before the photodetector to vary the received optical power. If the photodetector does not have an integrated amplifier, an external amplifier is used to boost the signal before it is analyzed. BER is measured by an error analyzer which compares the sent and received bits. An oscilloscope may be used to record eye diagrams consisting of an overlay of many received data patterns. These may be used to measure jitter, rise and fall times, analyze overshoot as well as optimize the setup alignment and bias point before performing more time consuming BER measurements.

The VCSEL performance is determined by measuring the BER for different received powers, using the photodetector's built in monitor to record the received optical power. To accurately evaluate very low error-rates (BER $< 10^{-10}$) statistical methods are used where the BER is taken as the 95% confidence interval. The link is defined as error-free when the BER is less than 10^{-12} with a confidence of 95%.

Chapter 6

VCSEL Fabrication

The epitaxial VCSEL structures used in this work were grown by IQE Europe Ltd. using metal-organic chemical vapor deposition (MOCVD). Molecular beam epitaxty (MBE) can also be used to grow the structure, but MOCVD is usually preferred for commercial operation because of the higher throughput. In MOCVD gaseous organic compounds transport III-metals (Al, Ga, In) into the reactor where they react with gaseous As (carried by the gas AsH_3) and deposits on the heated substrate. Doping may be introduced by introducing Si or C into the reactor for n- and p-doping respectively. After the growth of the epitaxial structure, the device processing starts. The different processing steps used in high-speed VCSEL fabrication will now be briefly described, followed by and overview of the full process. Details about the VCSEL processes can be found in appendix A.

6.1 Lithography

Most process steps in nanofabrication starts by patterning a protective coating called a resist on the sample using lithography. The most straightforward method is photolithography where a photoresist (a photosensitive polymer diluted with a solvent) is used. The viscous photoresist is dispensed onto the sample which is spun at a few thousand rounds per minute to form a thin film. The film thickness is on the order of one or a few micrometers depending on the resist viscosity and spin speed. The resist is then baked on a hotplate to remove the solvent. To pattern the resist a glass plate with a chromium pattern is manually aligned on top of the sample, shadowing certain areas as the sample is exposed with ultra-violet radiation at 400 nm. By using a liquid

developer, the exposed areas may be removed leaving a pattern on the sample. The manual alignment has an error margin of around 1 µm. If a so-called negative resist is being used, the unexposed resist areas are instead removed. A third resist type is image reversal resist, commonly used for lift-off processes.

The wave nature of light prohibits definition of features smaller than $\lambda/2$ by conventional photolithography. Standard contact photolithography with a resolution of approximately 1 µm, was used in this work [77]. More advanced photolithography techniques such as phase shifted masks, enables the definition of features smaller than 100 nm. However, such a process is not feasible for a flexible research environment. Electron beam lithography is used instead. It works essentially the same way as photolithography, but instead using an electron-sensitive resist. The main difference is that instead of a UV lamp exposing the entire sample as once, an electron beam scans across the sample, making this lithography technique a more time consuming serial process. Because of the very short electron wavelength, electron beam lithography can achieve a resolution down to 10 nm. The electron beam lithography system uses an automated alignment system that detects alignment marks on the sample for near perfect alignment. Definition of small features in commercial production may also be done by nanoimprint lithography, where an imprint resist is patterned with a stamp. Compared to the serial electron beam lithography, nanoimprint is very fast, but manufacturing of the stamp is expensive and it allows no process flexibility. This technique has for instance been used to fabricate polarization stable sub-wavelength grating VCSELs [78].

6.2 Thin Film Deposition

Both dielectric and metal thin films are used in VCSEL processing. Dielectric materials such as Si_xN_y (exact stoichiometry varies on processing conditions), SiO_2, amorphous Si and TiO_2 are commonly used as electrical passivation layers, hard masks and optical coatings as well as to protect surfaces during particular processing steps. Metal thin films are used for contacts on semiconductor material and bondpads. A lift-off process with an image-reversal photoresist is usually used for thin film deposition. After deposition the image reversal resist is lifted off by immersion in heated solvents (usually acetone, methanol and isopropanol). For difficult lift-offs acetone spray may be used, while ultrasonic bath should be avoided because of the risk of breaking the relatively brittle GaAs samples.

Dielectric materials are commonly deposited by plasma enhanced chemical vapor deposition (PECVD). Gases are injected into a vacuum chamber where a plasma is generated by for instance inductively coupled plasma (ICP). Ions and reactive radicals from the plasma react on the sample surface to form the thin film. The film thickness can be precisely in-situ monitored by a laser

interferometer. ICP-PECVD was used to deposit Si_xN_y to protect the top surface during oxidation and as a hardmask for mesa processing for mode filter VCSELs.

Metals thin films are conveniently deposited by electron beam evaporation. An electron beam is used to heat the metal which evaporates and is deposited on the sample. The deposition rate is accurately controlled by a software adjusting the electron beam current and monitoring the decrease in resonance frequency of a crystal as the deposited film thickness increases. This technique was used to deposit Ti/Pt/Au p-contacts and Ni/Ge/Au n-contacts.

Both dielectric and metal films can be deposited by sputtering. Energetic Ar ions generated in a plasma are accelerated towards a target and sputter away atoms which are deposited on the sample. Sputtering has the advantage of a better step coverage than PECVD and electron beam evaporation and was therefore used to deposit Ti/Au bondpads in this work.

6.3 Etching

Removal of semiconductor material may be done by either dry or wet etching, depending on the requirements on etch rate, anisotropy and selectivity. Wet etching is inherently chemical where a reactive liquid dissolves the material. GaAs wet etchants usually contains one oxidizer that oxidizes the surface and one acid that then dissolves the oxide. Even though a high selectivity can be achieved for certain material systems, the etched material usually etches isotropically, meaning that for instance a VCSEL mesa etched by wet etching would have sloped sidewalls.

When vertical sidewalls are desired, dry etching techniques are used. Ions and radicals are created in a plasma and accelerated towards the sample by an electric field, where the ions sputter away material and the highly reactive radicals chemically etch the material. This gives the dry etching process both a physical and a chemical etch component. By changing the process parameters the plasma density and accelerating electric field may be varied, meaning that the chemical and physical process components may be individually tuned in order to optimize the process. The etched material form volatile products that leave the process chamber through the vacuum exhaust. In this work inductively coupled plasma reactive ion etching (ICP-RIE) was used to etch AlGaAs (using $SiCl_4$/Ar and Cl_2/Ar), Si_xN_y (using NF_3) and benzocyclobutene (BCB, using CF_4/O_2). The dry etching is done in the same tool as the PECVD and the etch depth can be in-situ monitored with a laser interferometer.

To achieve a very precise etch depth for the surface relief mode filters, Ar ion beam milling was first used. Ar ions are generated in a plasma and accelerated towards the surface, sputtering away material. While the etch rate for ICP-RIE may vary due to different conditions that affect the sensitive

chemical component of the etch, the ion beam milling is purely physical. This enables a very stable and reproducible etch rate, allowing precise etch depths by timed etching. One drawback is that the etched material does not form volatile products, but may redeposit somewhere else on the sample. Papers C and D used Ar ion beam milling to etch the mode filters, while paper E used ICP-RIE using the laser interferometer for in-situ monitoring.

6.4 Wet Oxidation

In order to form the oxide aperture, the etched mesa sidewalls are exposed to hot water vapor at 420°C. Nitrogen gas is fed through a bubbler and carries the water vapor into a furnace. Through a glass window in the top of the furnace chamber, the oxidation can be in-situ observed by imaging the sample with an infrared LED through a microscope onto a CCD camera. The oxide apertures can be discerned by the difference in reflectivity between the oxidized and non-oxidized areas. The oxidation process is highly sensitive to the temperature and even a small temperature gradient across the sample will lead to a varying oxidation rate and an undesired spread in oxide apertures across the chip [52]. To avoid this, the chip can be turned 180° after half the process time. The oxidation rate for $Al_{0.98}Ga_{0.02}As$ is approximately 0.25 µm/min in our standard oxidation process. Layers with a lower Al content will oxidize much slower, but neighboring layers such as $Al_{0.90}Ga_{0.10}As$ may oxidize vertically from the 98% layer, making the oxide layer thicker, see figure 3.5.

6.5 High-Speed VCSEL Process

Before processing starts, the large 3" wafer is cleaved into 8 x 10 mm chips and cleaned. As a first step Ti/Pt/Au alignment marks and top p-contact rings are deposited by electron beam evaporation (figure 6.1a). Then a Si_xN_y film is blanket deposited to protect the top surface during the later wet oxidation step. The mesas are defined by electron beam or photolithography and etched using ICP-RIE to remove first the protective Si_xN_y (using NF_3) and then etch the AlGaAs with $Ar/SiCl_4$ and Ar/Cl_2. A precise etch depth of 3.3-3.5 µm is obtained by using an in-situ laser interferometer in order to expose the oxide layers, but not the AlAs layers of the bottom DBR. Without breaking vacuum, the sample is moved to another chamber where ICP-PECVD is used to deposit another layer Si_xN_y. After lifting off the photoresist, the chip will be covered in Si_xN_y without any AlGaAs being exposed to air (figure 6.1b). The Si_xN_y on the sidewalls is removed by photolithography and ICP-RIE etching with NF_3, which has a high selectivity ($\sim$100) to AlGaAs. The oxidation at 420°C takes around 40 min and is monitored using the in-situ microscope (figure 6.1c). By using different mesa sizes, oxide aperture diameters from 3 to 9 µm are

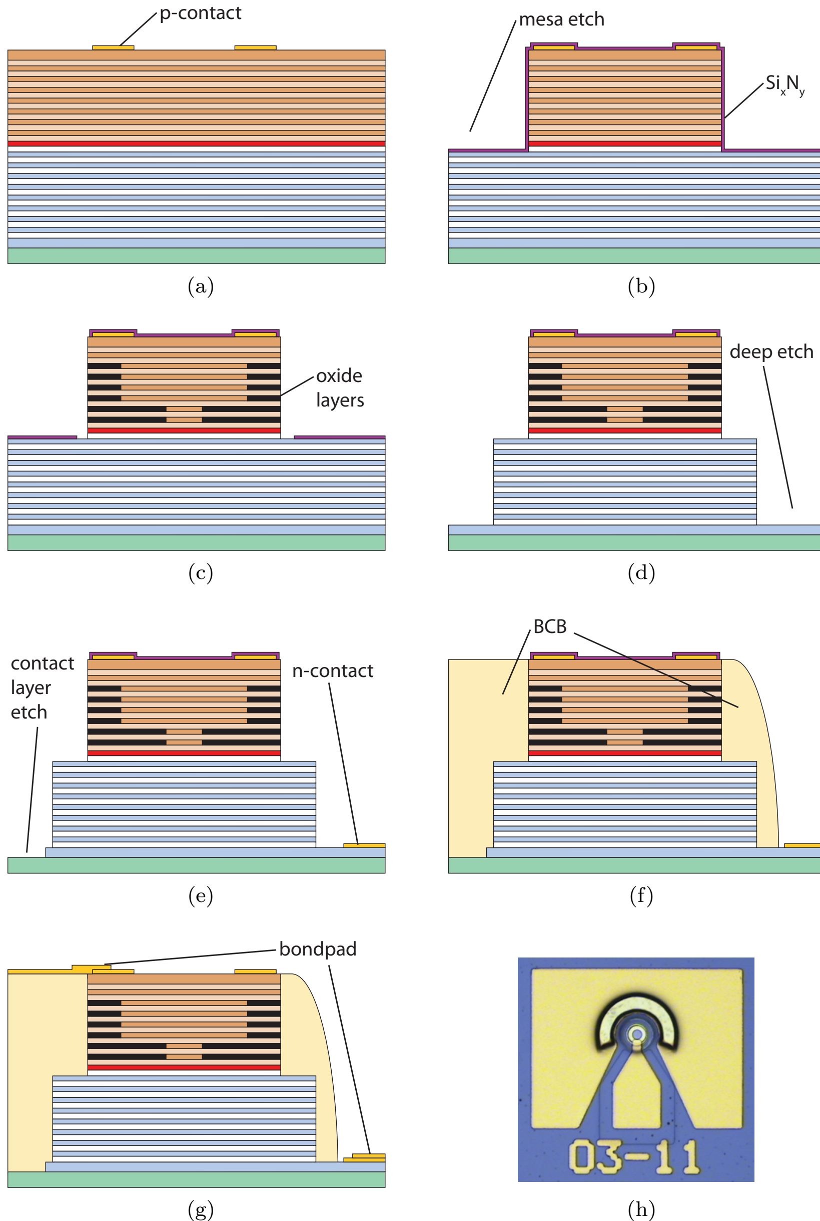

Figure 6.1: High-speed VCSEL process steps: (a) top contact evaporation, (b) mesa etch and Si_xN_y deposition, (c) open up Si_xN_y and wet oxidation, (d) deep etch, (e) bottom contact evaporation and contact layer etch, (f) BCB planarization and (g) bondpad deposition. (h) a microscope image of a finished high-speed VCSEL (courtesy of P. Westbergh).

obtained. After photolithography, the bottom mesa is etched to reach the n-contact layer, using again NF_3 to remove the Si_xN_y and Ar/$SiCl_4$ and Ar/Cl_2 to etch the AlGaAs (figure 6.1d).

The bottom Ni/Ge/Au n-contacts are deposited by electron beam evaporation and annealed for 30 s at 430°C in an N_2 atmosphere. Following this step the n-doped GaAs contact layer is removed under the future p-bondpad by photolithography and ICP-RIE etching (figure 6.1e). A thick layer of BCB is spun over the mesa to planarize the structure (figure 6.1f). The BCB is photosensitive enabling opening up of the BCB covering the n-contact and mesa by photolithography. However, spreading of the UV-light in the thick BCB prevents complete opening up by photolithography only, and the last BCB must be etched away using ICP-RIE etching with CF_4/O_2. It is very important to remove all BCB and at the same time not etch through the protective Si_xN_y. As final steps, the protective Si_xN_y is removed with ICP-RIE and Ti/Au bondpads are deposited by sputtering to achieve a good step coverage into the n-contact trench (figure 6.1g). More details are found in appendix A.

6.5.1 Surface Relief Processing

There are a few special requirements on the processing of mode filter VCSELs. Firstly, the epitaxial growth must have nm-precision in order to have an anti-phase top DBR reflection with a high loss. For the processing of the mode filter it is necessary to achieve good alignment between the oxide aperture and surface relief as well as a precise etch depth, see figure 4.2b. Near perfect alignment is obtained by using electron beam lithography to define the mode filters, aligned to etched alignment marks defined simultaneously with the mesas. Another option would be to use a self-aligned process, where the mesa edge (which will define the oxide aperture) and the mode filter is defined by a donut-shaped hard mask [73]. However, because of variations in oxide aperture due to a varying oxidation rate, the mode filters were defined and etched as the very last process step. This allowed matching of every oxide aperture with an appropriate mode filter. It is critical that the VCSEL top surface, with its anti-phase reflection, is carefully protected during the processing since accidental oxidation or etching of just a few nanometers will impact the mode filter performance.

Chapter 7

Outlook and Future Directions

Despite the last few years remarkable increase in the maximum reach of high-speed 850 nm VCSEL links, there are still much left to be investigated for better understanding how to design and fabricate even higher performance quasi-single mode VCSELs.

Since the MMF itself is more costly per unit length than SMF, the relative cost-benefit of using VCSEL based MMF links decreases for long distances. In addition, each MMF core today only carries one channel, while an installed long-reach SMF link can use (or be upgraded to) wavelength division multiplexing (WDM) for increased capacity. One solution could be to employ coarse WDM in a MMF link, with arrays of VCSELs with varying wavelengths. One way of realizing integrated multi-wavelength arrays is to use high-contrast grating (HCG) reflectors [79], but this has not yet been experimentally shown. Commercial implementation of MMF links much longer than 500 m might not become economically viable, depending on the future cost of MMF and SMF. However, quasi-single mode VCSELs for MMF links will still be required in order to increase the bit-rate of links up to 500 m. Since the next step after 25 Gbit/s is expected to be 40 Gbit/s, a logical next step would be to pursue quasi-single mode VCSELs capable of transmitting 40 Gbit/s over 500 m of MMF. The following points could be investigated in order to reach this goal.

- **New generation of high-speed VCSELs:** The long-reach transmission properties, using either the small oxide aperture or the mode filter technique, have not yet been investigated for the newest generation of high-speed VCSELs from Chalmers. These VCSELs have shown record bandwidth [41], enabling transmission at record-high bit-rates back-to-back [40]. This was possible by using a shorter $\lambda/2$ cavity and DBRs with

optimized doping and composition grading for reduced resistance. Mode filter integration on these devices, or the use of small oxide apertures, could further improve the maximum bit-rate of long-reach links.

- **Optimized mode filter loss:** As described in paper D, the surface etching of the mode filter has a significant influence on both static and dynamic properties. To obtain a better understanding of this complicated interplay, a parametric study of devices with varying surface relief diameter, and possibly etch depth, is desirable.
- **Reduced index guiding:** To achieve even higher output power, a larger oxide aperture is required (6-8 μm). This may need a lower effective index step, which might be possible by design simulations investigation of the placing, thickness and number of the oxide layers. The drawback is that thinner oxide layers increase the capacitance, lowering the parasitic roll-off frequency and reducing the VCSEL bandwidth.

Chapter 8

Summary of Papers

Paper A

"20 Gbit/s error-free operation of 850 nm oxide-confined VCSELs beyond 1 km of multimode fibre," *Electron. Lett.*, vol. 48, no. 19, pp. 1225-1227, Sept. 2012.

In this paper we present long-reach transmission using a small oxide aperture (∼3 µm) quasi-single mode VCSEL. With an RMS spectral width of 0.29 nm, error-free (BER $<10^{-12}$) transmission at 20 Gbit/s over 1.1 km of OM4 MMF was possible.

Paper B

"High-Speed 850 nm Quasi-Single-Mode VCSELs for Extended-Reach Optical Interconnects," *J. Opt. Commun. Netw.*, vol. 5, no. 7, pp. 686-695, July 2013.

This paper is an expanded investigation of small oxide aperture quasi-single mode VCSELs. The VCSEL dynamic properties were investigated by small-signal modulation measurements, giving a bandwidth of 23 GHz and a large D-factor of 17.3 GHz/mA$^{1/2}$. A 10 GHz photoreceiver with an integrated transimpedance amplifier was used to transmit up to 22 Gbit/s over 1100 m of OM4 MMF. A theoretical study of the influence of the receiver bandwidth on the link performance shows that a receiver with 15 GHz bandwidth should enable transmission at 25 Gbit/s over 1000 m. The calculations also indicate

that 2 km transmission at 20 Gbit/s could be possible with a receiver with >15 GHz bandwidth, but this also requires sufficient VCSEL output power to overcome fiber and connector losses.

Paper C

"25 Gbit/s transmission over 500 m multimode fibre using 850 nm VCSEL with integrated mode filter," *Electron. Lett.*, vol. 48, no. 9, pp. 517-518, April 2012.

The spectral width of high-speed VCSELs developed at Chalmers was reduced by integrating inverted surface relief mode filters. A significant reduction in RMS spectral width from 0.9 to 0.3 nm was obtained when etching a 1.5 µm diameter mode filter on a 5 µm oxide aperture VCSEL. The reduced effects of chromatic and modal fiber dispersion enabled error-free (BER $< 10^{-12}$) transmission at 25 Gbit/s over 500 m of OM3+ MMF.

Paper D

"Reducing the spectral width of high speed oxide confined VCSELs using an integrated mode filter," *Proceedings of SPIE Vertical-Cavity Surface-Emitting Lasers XVI*, vol. 8276, Feb. 2012.

This conference paper expands on the study from paper C with more details on device structure and mode filter functionality. Spectrally resolved near-field imaging was used to identify the different transverse modes and their relative radial intensity distributions of a large spectral width high-speed VCSEL. The static and dynamic properties of three different 5 μm-aperture VCSELs are compared; one with a surface relief mode filter, one without any surface etch (full anti-phase top DBR reflection) and one device with the entire surface etched to an in-phase reflection. As expected, the shallow surface etching has a significant influence on both static and dynamic properties.

Paper E

"20 Gb/s data transmission over 2 km multimode fibre using 850 nm mode filter VCSELs," *Manuscript*, Aug. 2013.

This manuscript contains very recent, not yet published results, for long-distance transmission using mode filter VCSELs. By using a 6 µm oxide aperture with 3 µm surface relief mode filter, single-mode output power exceeding 4 mW was achieved. This enabled error-free (BER $< 10^{-12}$) transmission at

25 and 20 Gbit/s over 1300 and 2000 m of OM4 MMF, respectively. The resulting bit-rate-distance product of 40 Gbit·km/s is the highest ever reported for directly modulated 850 nm VCSEL links.

References

[1] C. Kachris and I. Tomkos, "The rise of optical interconnects in data centre networks," In *Transparent Optical Networks (ICTON), 2012 14th International Conference on*, pages 1–4, 2012. doi:10.1109/ICTON.2012.6253903.

[2] A. Vahdat, H. Liu, X. Zhao, and C. Johnson, "The emerging optical data center," In *Optical Fiber Communication Conference and Exposition (OFC/NFOEC), 2011 and the National Fiber Optic Engineers Conference*, pages 1–3, 2011.

[3] F. Doany, "Power-Efficienty, High-Bandwidth Optical Interconnects for High Performance Computing," 2011.

[4] H. Liu, C. F. Lam, and C. Johnson, "Scaling Optical Interconnects in Datacenter Networks Opportunities and Challenges for WDM," In *High Performance Interconnects (HOTI), 2010 IEEE 18th Annual Symposium on*, pages 113–116, 2010. doi:10.1109/HOTI.2010.15.

[5] K. Iga, "Surface-emitting laser-its birth and generation of new optoelectronics field," *Selected Topics in Quantum Electronics, IEEE Journal of*, 6(6):1201–1215, 2000. doi:10.1109/2944.902168.

[6] H. Soda, K. ichi Iga, C. Kitahara, and Y. Suematsu, "GaInAsP/InP Surface Emitting Injection Lasers," *Japanese Journal of Applied Physics*, 18(12):2329–2330, 1979. doi:10.1143/JJAP.18.2329.

[7] F. Koyama, S. Kinoshita, and K. Iga, "Room-temperature continuous wave lasing characteristics of a GaAs vertical cavity surface-emitting laser," *Applied Physics Letters*, 55(3):221–222, 1989. doi:10.1063/1.101913.

[8] Y. H. Lee, J. L. Jewell, A. Scherer, S. L. McCall, J. P. Harbison, and L. T. Florez, "Room-temperature continuous-wave vertical-cavity single-

quantum-well microlaser diodes," *Electronics Letters*, 25(20):1377–1378, 1989. doi:10.1049/el:19890921.

[9] M. R. T. Tan, "Commercial applications of vertical cavity surface emitting lasers," In *Lasers and Electro-Optics, 2000. (CLEO 2000). Conference on*, page 201, 2000. doi:10.1109/CLEO.2000.906911.

[10] M. Freebody, "Lasers Evolve to Meet the Demands of Optical Communications," *Photonics Spectra*, 2012.

[11] R. Michalzik, editor. *VCSELs - Fundamentals, Technology and Applications of Vertical-Cavity Surface-Emitting Lasers*. Springer-Verlag Berlin Heidelberg, 2013.

[12] A. Mutig and D. Bimberg, "Progress on High-Speed 980 nm VCSELs for Short-Reach Optical Interconnects," *Advances in Optical Technologies*, 2011. doi:doi:10.1155/2011/290508.

[13] A. Kasukawa, "VCSEL Technology for Green Optical Interconnects," *Photonics Journal, IEEE*, 4(2):642–646, 2012. doi:10.1109/JPHOT.2012.2190723.

[14] K. Szczerba, M. Karlsson, P. A. Andrekson, and A. Larsson, "Intersymbol interference penalties for OOK and 4-PAM in short-range optical communications," In *Optical Fiber Communication Conference and Exposition and the National Fiber Optic Engineers Conference (OFC/NFOEC), 2013*, pages 1–3, 2013.

[15] K. Szczerba, P. Westbergh, J. Karout, J. S. Gustavsson, Å. Haglund, M. Karlsson, P. A. Andrekson, E. Agrell, and A. Larsson, "4-PAM for high-speed short-range optical communications," *Optical Communications and Networking, IEEE/OSA Journal of*, 4(11):885–894, 2012. doi:10.1364/JOCN.4.000885.

[16] K. Szczerba, P. Westbergh, M. Karlsson, P. A. Andrekson, and A. Larsson, "60 Gbits error-free 4-PAM operation with 850 nm VCSEL," *Electronics Letters*, 49(15):–, 2013. doi:10.1049/el.2013.1755.

[17] R. E. Freund, C. Bunge, N. N. Ledentsov, D. Molin, and C. Caspar, "High-Speed Transmission in Multimode Fibers," *Lightwave Technology, Journal of*, 28(4):569–586, 2010. doi:10.1109/JLT.2009.2030897.

[18] A. Gholami, D. Molin, and P. Sillard, "Compensation of Chromatic Dispersion by Modal Dispersion in MMF- and VCSEL-Based Gigabit Ethernet Transmissions," *Photonics Technology Letters, IEEE*, 21(10):645–647, 2009. doi:10.1109/LPT.2009.2015891.

[19] P. Westbergh, J. S. Gustavsson, Å. Haglund, A. Larsson, F. Hopfer, G. Fiol, D. Bimberg, and A. Joel, "32 Gbit/s multimode fibre transmission using high-speed, low current density 850 nm VCSEL," *Electronics Letters*, 45(7):366–368, 2009. doi:10.1049/el.2009.0201.

[20] Y. Liu, K. Johnson, and M. K. Hibbs-Brenner. "Chip-scale integration of vcsel, photodetector, and microlens arrays,", 2002. doi:10.1117/12.469564.

[21] Finisar. "Finisar C.wire,". Available online http://www.finisar.com/products/active-cables/C.wire accessed 2013-07-22, 2013.

[22] "Multimode Optical Fiber Selection & Specification,". Technical report, Corning Cable Systems LLC, 2012.

[23] D. Molin, M. Bigot-Astruc, and P. Sillard, "Chromatic dispersion compensated multimode fibers for data communications," In *Optical Communication (ECOC), 2011 37th European Conference and Exhibition on*, pages 1–3, 2011.

[24] J. King. "100m MMF reach objective baseline proposal - MMF ad HOC,". Available online http://www.ieee802.org/3/bm/public/jan13/king_02_0113_optx.pdf accessed 2013-08-02, 2013.

[25] I. T. Organization. "Infiniband Roadmap,". Available online http://www.infinibandta.org/content/pages.php?pg=technology_overview accessed 2013-08-02, 2013.

[26] F. Channel. "Fibre Channel Roadmaps,". Available online http://www.fibrechannel.org/fibre-channel-roadmaps.html accessed 2013-08-02, 2013.

[27] L. Qiu, E. Lawrence, B. Ayres, M. Schumacher, A. Amezcua, D. Molin, and G. Kuyt, "40GBASE-SR4 frame error rate test of chromatic dispersion compensating MMF," In *Optical Fiber Communication Conference and Exposition and the National Fiber Optic Engineers Conference (OFC/NFOEC), 2013*, pages 1–3, 2013.

[28] A. Gholami, D. Molin, and P. Sillard, "Physical Modeling of 10 GbE Optical Communication Systems," *Lightwave Technology, Journal of*, 29(1):115–123, 2011. doi:10.1109/JLT.2010.2095454.

[29] G. Giaretta, R. Michalzik, and A. J. Ritger, "Long distance (2.8 km), short wavelength (0.85 um) data transmission at 10Gb/sec over new generation high bandwidth multimode fiber," In *in Proc. Conference on Lasers and Electro-Optics, San Fransisco*, pages 683–684, 2000.

[30] P. Pepeljugoski, D. Kuchta, Y. Kwark, P. Pleunis, and G. Kuyt, "15.6-Gb/s transmission over 1 km of next generation multimode fiber," *Photonics Technology Letters, IEEE*, 14(5):717–719, 2002. doi:10.1109/68.998736.

[31] G. Fiol, J. A. Lott, N. N. Ledentsov, and D. Bimberg, "Multimode optical fibre communication at 25 Gbit/s over 300 m with small spectral-width 850 nm VCSELS," *Electronics Letters*, 47(14):810–811, 2011. doi:10.1049/el.2011.1148.

[32] P. Westbergh, J. S. Gustavsson, B. Kögel, Å. Haglund, A. Larsson, A. Mutig, A. Nadtochiy, D. Bimberg, and A. Joel, "40 Gbit/s error-free operation of oxide-confined 850 nm VCSEL," *Electronics Letters*, 46(14):1014–1016, 2010. doi:10.1049/el.2010.1405.

[33] P. Moser, J. A. Lott, P. Wolf, G. Larisch, A. Payusov, N. N. Ledentsov, W. Hofmann, and D. Bimberg, "99 fJ/(bit · km) Energy to Data-Distance Ratio at 17 Gb/s Across 1 km of Multimode Optical Fiber With 850-nm Single-Mode VCSELs," *Photonics Technology Letters, IEEE*, 24(1):19–21, 2012. doi:10.1109/LPT.2011.2171938.

[34] J.-W. Shi, J.-C. Yan, J.-M. Wun, J. Chen, and Y.-J. Yang, "Oxide-Relief and Zn-Diffusion 850-nm Vertical-Cavity Surface-Emitting Lasers With Extremely Low Energy-to-Data-Rate Ratios for 40 Gbit/s Operations," *Selected Topics in Quantum Electronics, IEEE Journal of*, 19(2):7900208–7900208, 2013. doi:10.1109/JSTQE.2012.2210863.

[35] P. Moser, J. A. Lott, P. Wolf, G. Larisch, A. Payusov, N. N. Ledentsov, and D. Bimberg, "Energy-Efficient Oxide-Confined 850-nm VCSELs for Long-Distance Multimode Fiber Optical Interconnects," *Selected Topics in Quantum Electronics, IEEE Journal of*, 19(2):7900406–7900406, 2013. doi:10.1109/JSTQE.2012.2218795.

[36] P. Westbergh, R. Safaisini, E. Haglund, J. S. Gustavsson, A. Larsson, M. Geen, R. Lawrence, and A. Joel, "High-Speed Oxide Confined 850-nm VCSELs Operating Error-Free at 40 Gb/s up to 85°C," *Photonics Technology Letters, IEEE*, 25(8):768–771, 2013. doi:10.1109/LPT.2013.2250946.

[37] P. Moser, P. Wolf, G. Larisch, J. A. Lott, and D. Bimberg, "Energy efficient 850 nm VCSELs for Data and Computer Communication," In *European VCSEL Day 2013*, 2013.

[38] M. Tan, S. Fryslie, J. A. Lott, N. N. Ledentsov, D. Bimberg, and K. Choquette, "Error-Free Transmission over 1-km OM4 Multimode Fiber at

25 Gb/s Using a Single Mode Photonic Crystal Vertical-Cavity Surface-Emitting Laser," *Photonics Technology Letters, IEEE*, PP(99):1–1, 2013. doi:10.1109/LPT.2013.2275351.

[39] P. Moser, J. A. Lott, P. Wolf, G. Larisch, H. Li, and D. Bimberg, "85-fJ Dissipated Energy Per Bit at 30 Gb/s Across 500-m Multimode Fiber Using 850-nm VCSELs," *Photonics Technology Letters, IEEE*, 25(16):1638–1641, 2013. doi:10.1109/LPT.2013.2273222.

[40] P. Westbergh, E. P. Haglund, E. Haglund, R. Safaisini, J. S. Gustavsson, and A. Larsson, "High-speed 850 nm VCSELs operating error free up to 57 Gbit/s," *Electronics Letters*, 49(16):–, 2013. doi:10.1049/el.2013.2042.

[41] P. Westbergh, R. Safaisini, E. Haglund, B. Kögel, J. S. Gustavsson, A. Larsson, M. Geen, R. Lawrence, and A. Joel, "High-speed 850 nm VCSELs with 28 GHz modulation bandwidth operating error-free up to 44 Gbit/s," *Electronics Letters*, 48(18):1145–1147, 2012. doi:10.1049/el.2012.2525.

[42] P. Moser, J. A. Lott, and D. Bimberg, "Energy Efficiency of Directly Modulated Oxide-Confined High Bit Rate 850-nm VCSELs for Optical Interconnects," *Selected Topics in Quantum Electronics, IEEE Journal of*, 19(4):1702212–1702212, 2013. doi:10.1109/JSTQE.2013.2255266.

[43] A. K. Eriksson, "Så mycket el drar Facebook i Luleå ," *Svenska Dagbladet*, 2013.

[44] C. Kachris and I. Tomkos, "A Survey on Optical Interconnects for Data Centers," *Communications Surveys Tutorials, IEEE*, 14(4):1021–1036, 2012. doi:10.1109/SURV.2011.122111.00069.

[45] J. E. Proesel, B. G. Lee, C. W. Baks, and C. L. Schow, "35-Gb/s VCSEL-Based optical link using 32-nm SOI CMOS circuits," In *Optical Fiber Communication Conference and Exposition and the National Fiber Optic Engineers Conference (OFC/NFOEC), 2013*, pages 1–3, 2013.

[46] B. Kögel, P. Debernardi, P. Westbergh, J. S. Gustavsson, Å. Haglund, E. Haglund, J. Bengtsson, and A. Larsson, "Integrated MEMS-Tunable VCSELs Using a Self-Aligned Reflow Process," *Quantum Electronics, IEEE Journal of*, 48(2):144–152, 2012. doi:10.1109/JQE.2011.2172191.

[47] S. Adachi, editor. *Properties of Aluminium Gallium Arsenide*. INSPEC, London, UK, 1993.

[48] M.-C. Amann and W. Hofmann, "InP-Based Long-Wavelength VCSELs and VCSEL Arrays," *Selected Topics in Quantum Electronics, IEEE Journal of*, 15(3):861–868, 2009. doi:10.1109/JSTQE.2009.2013182.

[49] E. Kapon, A. Sirbu, V. Iakovlev, A. Mereuta, A. Caliman, and G. Suruceanu, "Recent developments in long wavelength VCSELs based on localized wafer fusion," In *Transparent Optical Networks, 2009. ICTON '09. 11th International Conference on*, pages 1–4, 2009. doi:10.1109/ICTON.2009.5185024.

[50] R. N. Hall, G. E. Fenner, J. D. Kingsley, T. J. Soltys, and R. O. Carlson, "Coherent Light Emission From GaAs Junctions," *Phys. Rev. Lett.*, 9:366–368, 1962. doi:10.1103/PhysRevLett.9.366.

[51] S. B. Healy, E. P. O'Reilly, J. S. Gustavsson, P. Westbergh, Å. Haglund, A. Larsson, and A. Joel, "Active Region Design for High-Speed 850-nm VCSELs," *Quantum Electronics, IEEE Journal of*, 46(4):506–512, 2010. doi:10.1109/JQE.2009.2038176.

[52] K. D. Choquette, K. M. Geib, C. I. H. Ashby, R. D. Twesten, O. Blum, H. Q. Hou, D. M. Follstaedt, B. Hammons, D. Mathes, and R. Hull, "Advances in selective wet oxidation of AlGaAs alloys," *Selected Topics in Quantum Electronics, IEEE Journal of*, 3(3):916–926, 1997. doi:10.1109/2944.640645.

[53] B. Weigl, M. Grabherr, C. Jung, R. Jager, G. Reiner, R. Michalzik, D. Sowada, and K. J. Ebeling, "High-performance oxide-confined GaAs VCSELs," *Selected Topics in Quantum Electronics, IEEE Journal of*, 3(2):409–415, 1997. doi:10.1109/2944.605686.

[54] Y. Ou, J. S. Gustavsson, P. Westbergh, Å. Haglund, A. Larsson, and A. Joel, "Impedance Characteristics and Parasitic Speed Limitations of High-Speed 850-nm VCSELs," *Photonics Technology Letters, IEEE*, 21(24):1840–1842, 2009. doi:10.1109/LPT.2009.2034618.

[55] A. M. Nadtochiy, S. A. Blokhin, A. G. Kuzmenkov, M. Maksimov, N. A. Maleev, S. I. Troshkov, N. N. Ledentsov, V. M. Ustinov, A. Mutig, and D. Bimberg, "Decreasing parasitic capacitance in vertical-cavity surface-emitting laser with selectively oxidized aperture," *Technical Physics Letters*, 38(2):106–109, 2012. doi:10.1134/S1063785012020101.

[56] K. J. Ebeling. *Semiconductor Quantum Optoelectronics: From Quantum Physics to Smard Devices*, chapter Analysis of vertical cavity surface emitting laser diodes (VCSEL), pages 295–338. SUSSP Publications and Institute of Physics Publishing, 1999.

[57] B. E. A. Saleh and M. C. Teich. *Fundamentals of Photonics.* John Wiley & Sons, 2007.

[58] Y. Satuby and M. Orenstein, "Mode-coupling effects on the small-signal modulation of multitransverse-mode vertical-cavity semiconductor lasers," *Quantum Electronics, IEEE Journal of*, 35(6):944–954, 1999. doi:10.1109/3.766838.

[59] L. A. Coldren and S. W. Corzine. *Diode Lasers and Photonics Integrated Circuits.* John Wiley & Sons, 1995.

[60] P. Baveja, B. Kögel, P. Westbergh, J. S. Gustavsson, Å. Haglund, D. N. Maywar, G. P. Agrawal, and A. Larsson, "Impact of Device Parameters on Thermal Performance of High-Speed Oxide-Confined 850-nm VCSELs," *Quantum Electronics, IEEE Journal of*, 48(1):17–26, 2012. doi:10.1109/JQE.2011.2176554.

[61] P. Westbergh, J. S. Gustavsson, B. Kögel, Å. Haglund, and A. Larsson, "Impact of photon lifetime on high-speed VCSEL performance," *IEEE Journal of Selected Topics in Quantum Electronics*, 21(6):1603–1613, 2011. doi:10.1109/JSTQE.2011.2114642.

[62] P. Westbergh, J. S. Gustavsson, Å. Haglund, M. Sköld, A. Joel, and A. Larsson, "High-Speed, Low-Current-Density 850 nm VCSELs," *Selected Topics in Quantum Electronics, IEEE Journal of*, 15(3):694–703, 2009. doi:10.1109/JSTQE.2009.2015465.

[63] Å. Haglund, J. S. Gustavsson, J. Bengtsson, P. Jedrasik, and A. Larsson, "Design and evaluation of fundamental-mode and polarization-stabilized VCSELs with a subwavelength surface grating," *Quantum Electronics, IEEE Journal of*, 42(3):231–240, 2006. doi:10.1109/JQE.2005.863703.

[64] J. M. Ostermann, F. Rinaldi, P. Debernardi, and R. Michalzik, "VCSELs with enhanced single-mode power and stabilized polarization for oxygen sensing," *Photonics Technology Letters, IEEE*, 17(11):2256–2258, 2005. doi:10.1109/LPT.2005.858134.

[65] A. Larsson, "Advances in VCSELs for Communication and Sensing," *Selected Topics in Quantum Electronics, IEEE Journal of*, 17(6):1552–1567, 2011. doi:10.1109/JSTQE.2011.2119469.

[66] I. Kardosh, F. Demaria, F. Rinaldi, S. Menzel, and R. Michalzik, "High-Power Single Transverse Mode Vertical-Cavity Surface-Emitting Lasers With Monolithically Integrated Curved Dielectric Mirrors," *Photonics Technology Letters, IEEE*, 20(24):2084–2086, 2008. doi:10.1109/LPT.2008.2006687.

[67] C. Jung, R. Jager, M. Grabherr, P. Schnitzer, R. Michalzik, B. Weigl, S. Muller, and K. J. Ebeling, "4.8 mW singlemode oxide confined top-surface emitting vertical-cavity laser diodes," *Electronics Letters*, 33(21):1790–1791, 1997. doi:10.1049/el:19971207.

[68] B. Hawkins, R. A. I. Hawthorne, J. K. Guenter, J. A. Tatum, and J. R. Biard, "Reliability of various size oxide aperture VCSELs," In *Electronic Components and Technology Conference, 2002. Proceedings. 52nd*, pages 540–550, 2002. doi:10.1109/ECTC.2002.1008148.

[69] L. Y. Karachinsky, S. A. Blokhin, I. I. Novikov, N. A. Maleev, A. G. Kuzmenkov, M. A. Bobrov, J. A. Lott, N. N. Ledentsov, V. A. Shchukin, J.-R. Kropp, and D. Bimberg, "Reliability performance of 25 Gbit s^{-1} 850ănm vertical-cavity surface-emitting lasers," *Semiconductor Science and Technology*, 28(6):065010, 2013.

[70] H. Martinsson, J. A. Vukusic, and A. Larsson, "Single-mode power dependence on surface relief size for mode-stabilized oxide-confined vertical-cavity surface-emitting lasers," *Photonics Technology Letters, IEEE*, 12(9):1129–1131, 2000. doi:10.1109/68.874211.

[71] P. Dowd, L. Raddatz, Y. Sumaila, M. Asghari, I. White, R. V. Penty, P. Heard, G. C. Allen, R. Schneider, M. Tan, and S. Y. Wang, "Mode control in vertical-cavity surface-emitting lasers by post-processing using focused ion-beam etching," *Photonics Technology Letters, IEEE*, 9(9):1193–1195, 1997. doi:10.1109/68.618474.

[72] Å. Haglund, J. S. Gustavsson, J. Vukusic, P. Modh, and A. Larsson, "Single fundamental-mode output power exceeding 6 mW from VCSELs with a shallow surface relief," *IEEE Photonics Technology Letters*, 16(2):368–370, 2004. doi:10.1109/LPT.2003.821085.

[73] H. J. Unold, S. W. Z. Mahmoud, R. Jager, M. Grabherr, R. Michalzik, and K. J. Ebeling, "Large-area single-mode VCSELs and the self-aligned surface relief," *Selected Topics in Quantum Electronics, IEEE Journal of*, 7(2):386–392, 2001. doi:10.1109/2944.954155.

[74] J. M. Ostermann, P. Debernardi, C. Jalics, and R. Michalzik, "Polarization-stable oxide-confined VCSELs with enhanced single-mode output power via monolithically integrated inverted grating reliefs," *Selected Topics in Quantum Electronics, IEEE Journal of*, 11(5):982–989, 2005. doi:10.1109/JSTQE.2005.854145.

[75] A. Kroner, F. Rinaldi, J. M. Ostermann, and R. Michalzik, "High-performance single fundamental mode AlGaAs VCSELs with mode-

selective mirror reflectivities," *Optics Communications*, 270(2):332 – 335, 2007. doi:http://dx.doi.org/10.1016/j.optcom.2006.09.011.

[76] S. Arafin, A. Bachmann, K. Vizbaras, J. S. Gustavsson, A. Larsson, and M.-C. Amann, "Large-area single-mode GaSb-based VCSELs using an inverted surface relief," In *IEEE Photonics Society, 2010 23rd Annual Meeting of the*, pages 61–62, 2010. doi:10.1109/PHOTONICS.2010.5698757.

[77] R. Williams. *Mondern GaAs Processing Methods*. Artech House, Inc., 1990.

[78] M. A. Verschuuren, P. Gerlach, H. A. van Sprang, and A. Polman, "Improved performance of polarization-stable VCSELs by monolithic subwavelength gratings produced by soft nano-imprint lithography," *Nanotechnology*, 22(50):505201, 2011.

[79] V. Karagodsky, B. Pesala, C. Chase, W. Hofmann, F. Koyama, and C. J. Chang-Hasnain, "Monolithically integrated multi-wavelength VCSEL arrays using high-contrast gratings," *Opt. Express*, 18(2):694–699, 2010. doi:10.1364/OE.18.000694.

Appendix A

Process Plan

This is the process plan used for fabricating BCB planarized high-speed surface relief mode filter VCSELs. Small oxide aperture VCSELs may be fabricated by the same method, but preferably using photolithography instead for the mesa definition.

1. Cleave and Clean Sample

Use scriber to cleave 8 x 10 mm chips. Clean chips in warm acetone (50°C), methanol and IPA. Blow dry with nitrogen gas.

2. Photolithography for Alignment Marks and Top Contacts

Spin resist AZ5214E	4000 rpm for 30 s
Soft bake	110°C for 60 s on hot plate
Frame exposure	80 s in soft contact mode
Develop	40 s in AZ351B:H_2O (1:5), rinse in H_2O, blow dry with nitrogen gas
Pattern exposure	5 s in high pressure mode
Reversal bake	125°C for 60 s on hot plate
Flood exposure	80 s
Develop	20 s in AZ351B:H_2O (1:5), rinse in H_2O, blow dry with nitrogen gas
Ash	150 W O_2 plasma in barrel etcher

3. Evaporate Alignment Marks and Top Contacts

Remove surface oxides	HCl:H_2O (1:1) for 30 s
Ti deposition	100 Å at 2 Å/s
Pt deposition	200 Å at 1 Å/s
Au deposition	1500 Å at 4 Å/s
lift-off	Warm acetone, acetone spray, methanol and IPA, blow dry with nitrogen gas

4. Deposit Si_xN_y for Mesa Etch Mask, ICP-PECVD

a. Strike

Strike pressure	15 mTorr
Chamber pressure	0 mTorr (set point)
SiH_4	8 sccm
N_2	20 sccm
Ar	50 sccm
RF power	30 W
ICP power	120 W

b. Deposit

Chamber pressure	0 mTorr (set point)
SiH_4	8 sccm
N_2	20 sccm
Ar	50 sccm
RF power	1 W
ICP power	120 W
Time	∼19 min, 2.25 peaks, (monitor with laser interferometer)
Thickness	∼350 nm

5. Electron Beam Lithography for Mesa

Spin resist ZEP520A	3000 rpm for 30 s
Soft bake ramp	70-160°C (to avoid cracking Si_xN_y)
Soft bake	160°C for 5 min on hot plate
Pattern exposure	100 kV, 40 nA
Develop	90 s in n-amylacetate, rinse in IPA blow dry with nitrogen gas

5. Si_xN_y Mask Dry Etch, ICP-RIE

Chamber pressure	80 mTorr (set point)
NF_3	20 sccm
RF power	30 W
ICP power	300 W
Time	∼3 min, 2.25 peaks + 1 min overetch, (monitor with laser interferometer)
Etch depth	∼350 nm
Strip remaining resist	100 W O_2 plasma in batchtop etcher

6. Mesa Dry Etch, ICP-RIE

a. $SiCl_4$/Ar

Strike pressure	10 mTorr
Chamber pressure	0 mTorr (set point)
$SiCl_4$	10 sccm
Ar	20 sccm
RF power	55 W
ICP power	30 W
Time	~20 min, etch 24 peaks, (monitor with laser interferometer)
Etch depth	~2.4 µm

b. Cl_2/Ar

Strike pressure	10 mTorr
Chamber pressure	0 mTorr (set point)
Cl_2	20 sccm
Ar	10 sccm
RF power	75 W
ICP power	40 W
Time	~30 s, etch 3.5 peaks, (monitor with laser interferometer)
Etch depth	~0.35 µm

c. Ar clean

Strike pressure	10 mTorr
Chamber pressure	0 mTorr (set point)
Ar	20 sccm
RF power	50 W
ICP power	50 W
Time	1 min
Etch depth	<50 nm

7. Deposit Si_xN_y to Protect Surface, ICP-PECVD

This is done without breaking vacuum from the mesa etch.

a. Strike

Strike pressure	15 mTorr
Chamber pressure	0 mTorr (set point)
SiH_4	8 sccm
N_2	20 sccm
Ar	50 sccm
RF power	30 W
ICP power	120 W

b. Deposit

Chamber pressure	0 mTorr (set point)
SiH_4	8 sccm
N_2	20 sccm
Ar	50 sccm
RF power	1 W
ICP power	120 W
Time	~9 min, 1 peak, (monitor with laser interferometer)
Thickness	~170 nm

8. Photolithography to Open up Si_xN_y

Spin HMDS	4000 rpm for 30 s
Spin resist AZ4562	6000 rpm for 30 s carefully remove edge beads with tool
Soft bake ramp	60-100°C (to avoid cracking Si_xN_y)
Soft bake	110°C for 3 min on hot plate
Frame exposure	4 min in soft contact mode
Develop	4 min in AZ351B:H_2O (1:4), rinse in H_2O, blow dry with nitrogen gas
Pattern exposure	60 s in high pressure mode
Develop	1:45 min in AZ351B:H_2O (1:4), rinse in H_2O, blow dry with nitrogen gas
Ash	150 W O_2 plasma in barrel etcher

9. Open up Si_xN_y on Sidewalls, ICP-RIE

Chamber pressure	80 mTorr (set point)
NF_3	20 sccm
RF power	30 W
ICP power	300 W
Time	∼2 min, 1 peaks + 1 min overetch, (monitor with laser interferometer)
Etch depth	∼170 nm
Strip remaining resist	warm acetone, methanol and IPA

10. Wet Oxidation

Illumination wavelength	940 nm
N_2 flowmeter	120 ml
Water temperature	95°
Pipe temperature	150°
Furnace temperature	420°
Oxidation rate	∼0.25 µm/min
Time	∼40 min, (monitor through IR microscope)

11. Photolithography to Open up Si_xN_y

Spin HMDS	4000 rpm for 30 s
Spin resist AZ4562	6000 rpm for 30 s carefully remove edge beads with tool
Soft bake ramp	60-100°C (to avoid cracking Si_xN_y)
Soft bake	110°C for 3 min on hot plate
Frame exposure	4 min in soft contact mode
Develop	4 min in AZ351B:H_2O (1:4), rinse in H_2O, blow dry with nitrogen gas
Pattern exposure	60 s in high pressure mode
Develop	1:45 min in AZ351B:H_2O (1:4), rinse in H_2O, blow dry with nitrogen gas
Ash	150 W O_2 plasma in barrel etcher

12. Mesa Deep Etch, ICP-RIE

a. NF_3	(To remove Si_xN_y)
Chamber pressure	80 mTorr (set point)
NF_3	20 sccm
RF power	30 W
ICP power	300 W
Time	∼2 min, 1 peaks + 1 min overetch, (monitor with laser interferometer)
Etch depth	∼170 nm
Strip remaining resist	warm acetone, methanol and IPA
b. $SiCl_4$/Ar	
Strike pressure	10 mTorr
Chamber pressure	0 mTorr (set point)
$SiCl_4$	10 sccm
Ar	20 sccm
RF power	55 W
ICP power	30 W
Time	∼20 min, etch 22 peaks, (monitor with laser interferometer)
Etch depth	∼2.2 µm
c. Cl_2/Ar	
Strike pressure	10 mTorr
Chamber pressure	0 mTorr (set point)
Cl_2	20 sccm
Ar	10 sccm
RF power	75 W
ICP power	40 W
Time	∼30 s, etch 8 peaks +30 s, (monitor with laser interferometer)
Etch depth	∼0.35 µm
Strip remaining resist	warm acetone, methanol and IPA

13. Photolithography for n-Contact

Spin HMDS	4000 rpm for 30 s
Spin resist AZ4562	3000 rpm for 30 s, carefully remove edge beads with tool
Wait	>15 min to allow bubbles to escape
Soft bake	110°C for 4 min on hot plate
Frame exposure	4 min in soft contact mode
Develop	5 min in AZ351B:H_2O (1:4), rinse in H_2O, blow dry with nitrogen gas
Pattern exposure	2 min in soft contact mode
Wait	>15 min to allow bubbles to escape
Develop	3 min in AZ351B:H_2O (1:4), rinse in H_2O, blow dry with nitrogen gas
Ash	150 W O_2 plasma in barrel etcher

14. Evaporate n-Contact

Remove surface oxides	$HCl:H_2O$ (1:1) for 30 s
Ni deposition	200 Å at 1 Å/s
Ge deposition	520 Å at 1.5 Å/s
Au deposition	1000 Å at 4 Å/s
lift-off	Warm acetone, acetone spray, methanol and IPA, blow dry with nitrogen gas

15. Annealing of n-Contact

Temperature	430°
Ramp rate	10°/s
Time	30 s

16. Photolithography for Contact Layer Etch

Spin HMDS	4000 rpm for 30 s
Spin resist AZ4562	3000 rpm for 30 s carefully remove edge beads with tool
Wait	>15 min to allow bubbles to escape
Soft bake	110°C for 4 min on hot plate
Frame exposure	4 min in soft contact mode
Develop	5 min in $AZ351B:H_2O$ (1:4), rinse in H_2O, blow dry with nitrogen gas
Pattern exposure	2 min in soft contact mode
Wait	>15 min to allow bubbles to escape
Develop	3 min in $AZ351B:H_2O$ (1:4), rinse in H_2O, blow dry with nitrogen gas
Ash	150 W O_2 plasma in barrel etcher

17. Deep Etch, ICP-RIE

a. $SiCl_4/Ar$

Strike pressure	10 mTorr
Chamber pressure	0 mTorr (set point)
$SiCl_4$	10 sccm
Ar	20 sccm
RF power	55 W
ICP power	30 W
Time	~2 min (monitor with laser interferometer)
Etch depth	~0.3 µm

b. Cl_2/Ar

Strike pressure	10 mTorr
Chamber pressure	0 mTorr (set point)
Cl_2	20 sccm
Ar	10 sccm
RF power	75 W
ICP power	40 W
Time	~1:30 min (monitor with laser interferometer)
Etch depth	~0.7 µm

Strip remaining resist	warm acetone, methanol and IPA

18. Deposit Si_xN_y for Surface Protection, ICP-PECVD

a. Strike

Strike pressure	15 mTorr
Chamber pressure	0 mTorr (set point)
SiH_4	8 sccm
N_2	20 sccm
Ar	50 sccm
RF power	30 W
ICP power	120 W

b. Deposit

Chamber pressure	0 mTorr (set point)
SiH_4	8 sccm
N_2	20 sccm
Ar	50 sccm
RF power	1 W
ICP power	120 W
Time	~9 min, 1 peaks, (monitor with laser interferometer)
Thickness	~170 nm

19. Planarize Mesa with BCB

AP3000	3000 rpm for 30 s
BCB 4026-26	~2500 rpm for 30 s (may need calibration for old BCB)
Spin dry	3000 rpm for 30 s carefully remove edge beads with swab and DS2100
Soft bake	85° for 90 s on hot plate
Pattern expose	100 s in soft contact mode
Puddle develop	70 s in DS2100
Spin dry	3000 rpm for 30 s
Post bake	90° for 60 s on hot plate
Hard cure	260° for 60 min in oxygen free environment

20. Dry Etch BCB to Expose n-Contact and Mesa, ICP-RIE

Strike pressure	10 mTorr
Chamber pressure	10 mTorr (set point)
CF_4	10 sccm
O_2	40 sccm
RF power	50 W
ICP power	400 W
Time	~1 min check in microscope; repeat etch until BCB is gone, too long etch steps may burn BCB

21. Remove remaining Si_xN_y, ICP-RIE

Chamber pressure	80 mTorr (set point)
NF_3	20 sccm
RF power	30 W
ICP power	300 W
Time	~3 min, <1 peak + 30 s overetch, (monitor with laser interferometer)
Etch depth	<170 nm

22. Photolithography for Bondpads

Spin resist AZ5214E	3000 rpm for 30 s
Soft bake	110°C for 60 s on hot plate
Frame exposure	80 s in soft contact mode
Develop	40 s in AZ351B:H_2O (1:5), rinse in H_2O, blow dry with nitrogen gas
Pattern exposure	5 s in high pressure mode
Reversal bake	125°C for 60 s on hot plate
Flood exposure	80 s
Develop	20 s in AZ351B:H_2O (1:5), rinse in H_2O, blow dry with nitrogen gas
Ash	150 W O_2 plasma in barrel etcher

23. Sputter Bondpads

Substrate cleaning	30 sccm Ar, 7 mTorr, 50 W RF, 30 s
Ti traget cleaning	30 sccm Ar, 7 mTorr, 200 W DC, 60 s
Ti deposition	30 sccm Ar, 7 mTorr, 200 W DC, 20 s
Au traget cleaning	30 sccm Ar, 7 mTorr, 40 W DC, 30 s
Au deposition	30 sccm Ar, 7 mTorr, 40 W DC, 5:30 min
lift-off	Warm acetone, acetone spray, methanol and IPA, blow dry with nitrogen gas

24. Electron Beam Lithography for Surface Relief

Spin resist ZEP520A:anisole (1:1)	5000 rpm for 30 s
Soft bake ramp	70-160°C (to avoid cracking Si_xN_y)
Soft bake	160°C for 5 min on hot plate
Pattern exposure	100 kV, 10 nA
Develop	30 s in n-amylacetate, rinse in IPA blow dry with nitrogen gas

25a. Surface Relief Etch, Ion Beam Milling

Ar Beam current	20 mA
Beam voltage	300 V
Acceleration voltage	385 V
Neutralization current	30 mA
Ar	6 sccm
Ar neutralizer	6 sccm
Time	$\sim$6:30 min, (calibrate first on test piece)
Etch depth	59$\pm$5 nm

25b. Surface Relief Etch, ICP-RIE

Strike pressure	10 mTorr
Chamber pressure	2 mTorr (set point)
$SiCl_4$	4 sccm
Ar	30 sccm
RF power	50 W
ICP power	0 W
Time	$\sim$2:20 min, $\sim$0.6 peaks, monitor by using interferometer, run several calibration runs
Etch depth	59$\pm$5 nm